The CEBAF Large Acceptance Spectrometer (CLAS)

B.A. Mecking [a], G. Adams [b], S. Ahmad [c], E. Anciant [d], M. Anghinolfi [e], B. Asavapibhop [f], G. Asryan [g], G. Audit [d], T. Auger [d], H. Avakian [a,h], J.P. Ball [i], F.J. Barbosa [a], S. Barrow [j], M. Battaglieri [e], K. Beard [k,ℓ], B.L. Berman [m], N. Bianchi [h], S. Boiarinov [a], P. Bonneau [a], W.J. Briscoe [m], W.K. Brooks [a], V.D. Burkert [a], D.S. Carman [n], T. Carstens [a], C. Cetina [m], S.B. Christo [a], P.L. Cole [o,a], A. Coleman [ℓ,1], J. Connelly [m,2], D. Cords [a,3], P. Corvisiero [e], D. Crabb [p], H. Crannell [q], R.C. Cuevas [a], P.V. Degtyarenko [a], L. Dennis [j], E. DeSanctis [h], R. DeVita [e], J. Distelbrink [r], G.E. Dodge [s], W. Dodge [m,3], G. Doolittle [a], D. Doughty [t,a], M. Dugger [i], W.S. Duncan [s], S. Dytman [u], H. Egiyan [ℓ], K.S. Egiyan [g], L. Elouadrhiri [a,t], R.J. Feuerbach [v], J. Ficenec [w], V. Frolov [b], H. Funsten [ℓ], G.P. Gilfoyle [x], K.L. Giovanetti [k], E. Golovatch [e,4], J. Gram [a], M. Guidal [y], V. Gyurjyan [a,n,h], D. Heddle [t,a], P. Hemler [a], F.W. Hersman [r], K. Hicks [n], R.S. Hicks [f], M. Holtrop [r], C.E. Hyde-Wright [s], D. Insley [a], M.M. Ito [a], G. Jacobs [a], D. Jenkins [w], K. Joo [a], D. Joyce [a], D. Kashy [a], M. Khandaker [z], W. Kim [aa], A. Klein [s], F.J. Klein [q,ab,a], M. Klusman [b], M. Kossov [ac], L. Kramer [ab], V. Koubarovski [b], S.E. Kuhn [s], A. Lake [a,5], D. Lawrence [f,i], A. Longhi [q], K. Lukashin [q,a,w], J. Lachniet [v], R.A. Magahiz [v], W. Major [x], J.J. Manak [a], C. Marchand [d], C. Martin [s], S.K. Matthews [q], M. McMullen [a], J.W.C. McNabb [v], M.D. Mestayer [a], R. Minehart [p], M. Mirazita [h], R. Miskimen [f], V. Muccifora [h], J. Mueller [u], L.Y. Murphy [m], G.S. Mutchler [ad], J. Napolitano [b], I. Niculescu [m], B.B. Niczyporuk [a], M. Nozar [a], J.T. O'Brien [q], A.K. Opper [n], J.E. O'Meara [a,5], E. Pasyuk [i], S.A. Philips [m], E. Polli [h], J.W. Price [ae,b], S. Pozdniakov [a], L.M. Qin [s], B.A. Raue [ab,a], G. Riccardi [j], G. Ricco [e], C. Riggs [a], M. Ripani [e],

B.G. Ritchie [i], J. Robb [a,5], F. Ronchetti [h,af], P. Rossi [h], F. Roudot [a], C. Salgado [z], V. Sapunenko [e], R.A. Schumacher [v], V.S. Serov [ac], Y.G. Sharabian [a,g], E.S. Smith [a,*], L.C. Smith [p], T. Smith [r,6], D.I. Sober [q], A. Stavinsky [ac], S. Stepanyan [s,t,g,a], P. Stoler [b], M. Taiuti [e], W.M. Taylor [a], S. Taylor [ad], D.J. Tedeschi [ag,u], U. Thoma [a], R. Thompson [u], D. Tilles [a], L. Todor [v], T.Y. Tung [ℓ], W. Tuzel [a,7], M.F. Vineyard [x], A.V. Vlassov [ac], L.B. Weinstein [s], R.E. Welsh [ℓ,a], D.P. Weygand [a], G.R. Wilkin [v], M. Witkowski [b], E. Wolin [a], A. Yegneswaran [a], P. Yergin [b,5], J. Yun [s]

[a] *Thomas Jefferson National Accelerator Facility, Newport News, Virginia 23606*

[b] *Rensselaer Polytechnic Institute, Troy, New York 12180*

[c] *Baylor College of Medicine, Houston, Texas 77030*

[d] *CEA-Saclay, Service de Physique Nucléaire, F91191 Gif-sur-Yvette, France*

[e] *INFN, Sezione di Genova, 16146 Genova, Italy*

[f] *University of Massachusetts, Amherst, Massachusetts 01003*

[g] *Yerevan Physics Institute, 375036 Yerevan, Armenia*

[h] *INFN, Laboratori Nazionali di Frascati, Frascati, Italy*

[i] *Arizona State University, Tempe, Arizona 85287*

[j] *Florida State University, Tallahassee, Florida 32306*

[k] *James Madison University, Harrisonburg, Virginia 22807*

[ℓ] *College of Willliam and Mary, Williamsburg, Virginia 23187*

[m] *The George Washington University, Washington, D.C. 20052*

[n] *Ohio University, Athens, Ohio 45701*

[o] *University of Texas at El Paso, El Paso, Texas 79968*

[p] *University of Virginia, Charlottesville, Virginia 22901*

[q] *Catholic University of America, Washington, D.C. 20064*

[r] *University of New Hampshire, Durham, New Hampshire 03824*

[s] *Old Dominion University, Norfolk, Virginia 23529*

[t] *Christopher Newport University, Newport News, Virginia 23606*

[u] *University of Pittsburgh, Pittsburgh, Pennsylvania 15260*

[v] *Carnegie Mellon University, Pittsburgh, Pennsylvania 15213*

[w] *Virginia Polytechnic Institute and State University, Blacksburg, Virginia 24061*

[x] *University of Richmond, Richmond, Virginia 23173*

[y] *Institut de Physique Nucléaire d'Orsay, IN2P3, BP 1, 91406 Orsay, France*

[z] *Norfolk State University, Norfolk, Virginia 23504*

[aa] *Kyungpook National University, Daegu 702-701, South Korea*
[ab] *Florida International University, Miami, Florida 33199*
[ac] *Institute of Theoretical and Experimental Physics, Moscow, 117259, Russia*
[ad] *Rice University, Houston, Texas 77005*
[ae] *University of California at Los Angeles, Los Angeles, California 90095*
[af] *Universitá di ROMA III, 00146 Roma, Italy*
[ag] *University of South Carolina, Columbia, South Carolina 29208*

Abstract

The CEBAF Large Acceptance Spectrometer (CLAS) is used to study photo- and electro-induced nuclear and hadronic reactions by providing efficient detection of neutral and charged particles over a good fraction of the full solid angle. A collaboration of about thirty institutions has designed, assembled, and commissioned CLAS in Hall B at the Thomas Jefferson National Accelerator Facility. The CLAS detector is based on a novel six-coil toroidal magnet which provides a largely azimuthal field distribution. Trajectory reconstruction using drift chambers results in a momentum resolution of 0.5% at forward angles. Cerenkov counters, time-of-flight scintillators, and electromagnetic calorimeters provide good particle identification. Fast triggering and high data acquisition rates allow operation at a luminosity of 10^{34} nucleon $cm^{-2}s^{-1}$. These capabilities are being used in a broad experimental program to study the structure and interactions of mesons, nucleons, and nuclei using polarized and unpolarized electron and photon beams and targets. This paper is a comprehensive and general description of the design, construction and performance of CLAS.

* Corresponding author: elton@jlab.org.
[1] Current address: Systems Planning and Analysis, Alexandria, Virginia 22311.
[2] Current address: Cisco, Washington, D.C. 20052.
[3] Current address: Deceased.
[4] Current address: Moscow State University, General Nuclear Physics Institute, 119899 Moscow, Russia.
[5] Current address: Retired.
[6] Current address: MIT-Bates Linear Accelerator Center, Middleton, Massachusetts 01949.
[7] Current address: Los Alamos National Laboratory, Los Alamos, New Mexico 87545.

Contents

PACS:
Keywords: CLAS, magnetic spectrometer, electromagnetic physics, large acceptance, JLab

1 Introduction

Electron scattering as a probe of the internal structure of nucleons and nuclei has been employed since the 1950's, mostly in inclusive reactions and using low-duty-cycle machines. Experiments in the deep inelastic regime revealed the quark sub-structure of the nucleon, and more recently showed that the spin structure of the nucleon is more complicated than originally anticipated.

A more detailed understanding of the structure of nucleons and nuclei requires the measurement of exclusive channels. For example, the study of the excited states of the nucleon requires the identification of spin, parity, and isospin of a state, which can only be accomplished by studying the resonance decay channels, and therefore requires exclusive measurements. In the past, low duty cycle machines have limited exclusive experiments to a few processes, mostly single pion production, and to restricted kinematics.

The construction of high-current, high-duty-cycle electron accelerators has changed this situation in a significant way. Electromagnetic processes may now be studied with statistical sensitivities comparable to hadronic reactions. This brings to bear the full capability of the electromagnetic interaction as a probe of the internal structure of hadrons and nuclei.

Large-acceptance detection is required to achieve high detection efficiency for multi-particle final states that are typical of reactions involving the production of excited mesons and baryons, as well as in nuclear break-up reactions. In addition, experiments may require a large-acceptance detector to compensate for various restrictions which limit their operation to moderate luminosity. For example, in experiments using a tagged bremsstrahlung photon beam, a low luminosity is required to keep accidental coincidences low. Also, solid-state polarized targets can only be operated at low beam currents, corresponding to low luminosity. A high detection efficiency for multi-particle events and a useful event rate at limited luminosity both require a detection system with a large acceptance.

Large acceptance detectors have been used routinely in combination with tagged-bremsstrahlung photon beams; examples are TAGX [1], SAPHIR [2], and DAPHNE [3]. The instantaneous photon beam intensity of a tagged photon beam is limited to approximately 10^7 tagged photons/s by accidental coincidences, typically resulting in relatively low background rates in a large-acceptance detector.

No such simple limitation exists for fixed-target electron-scattering experiments, therefore, the luminosity that can be handled by a large-acceptance detector will be limited by other factors, e.g. by a large electromagnetic background causing a high occupancy of the detector elements. Examples for large-

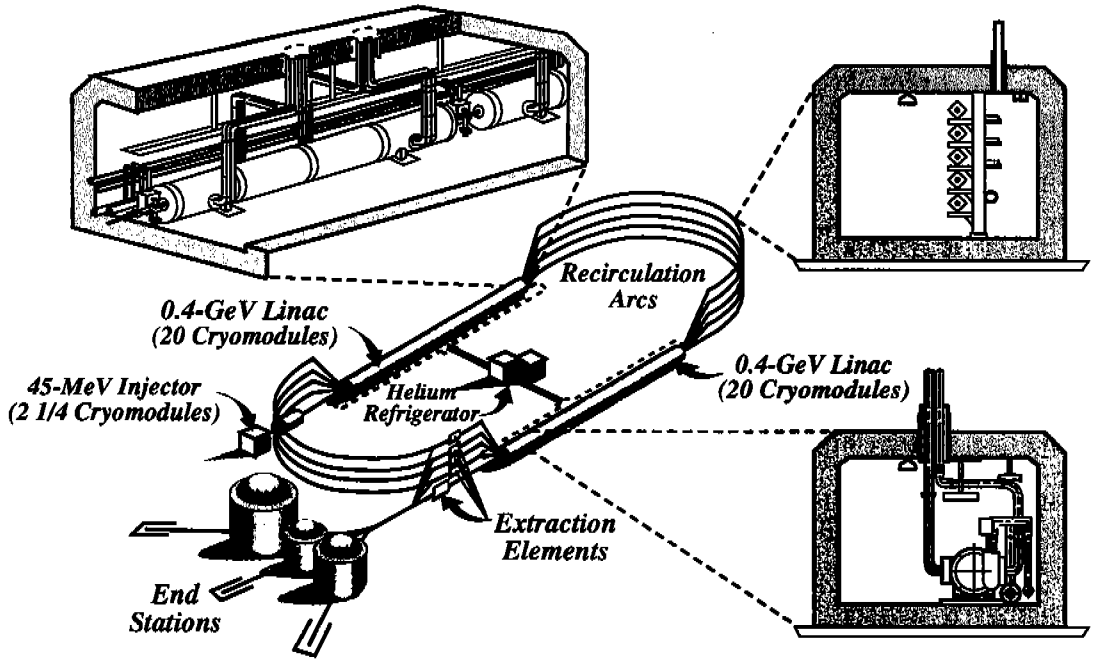

Fig. 1. Schematic layout of the CEBAF accelerator.

acceptance detectors using an electron beam include the LAME detector [4] that was operated at the Cornell 12-GeV electron synchrotron at an instantaneous luminosity of 3.2×10^{32} cm^{-2}s^{-1} and the HERMES detector [5] for fixed target experiments at HERA that is running at 5×10^{31} cm^{-2}s^{-1} for polarized targets (limited by the practical target densities) and 4×10^{33} cm^{-2}s^{-1} for unpolarized targets.

In this paper we will describe the design, construction and capabilities of CLAS, a novel large-acceptance detector for nuclear physics.

2 The Facility

The Continuous Electron Beam Accelerator Facility (CEBAF) at the Department of Energy's Thomas Jefferson National Accelerator Facility (Jefferson Lab) is devoted to the investigation of the electromagnetic structure of mesons, nucleons, and nuclei using high power electron and photon beams with energies up to 6 GeV and 100% duty cycle. A schematic of the accelerator and experimental halls is shown in Fig. 1. The primary electron beam from the CEBAF accelerator can be separated and sent to three different experimental areas, Halls A, B, and C, for simultaneous experiments. The experimental equipment in the halls is complementary, addressing a wide range of physics issues. Hall A has two identical focusing high-resolution spectrometers with a maximum momentum of 4 GeV/c [6]. Hall C has two symmetric focusing spec-

trometers: one featuring acceptance of high-momentum particles, the other a short path length for the detection of decaying particles [7]. Hall B houses the CEBAF Large Acceptance Spectrometer, CLAS, which was designed for operation with both electron and tagged-photon beams and is described in this article.

The CEBAF accelerator routinely delivers beam currents sufficient to achieve luminosities of several times 10^{38} $cm^{-2}s^{-1}$ to Halls A and C. The maximum luminosity of a large-acceptance detector is limited by detector occupancies to much lower values. This poses a challenge to routine accelerator operations in which the beam current to Hall B is frequently four orders of magnitude smaller than that simultaneously delivered to the other halls.

A broad physics program requiring large-acceptance particle detection is underway with CLAS. This program includes, among others, a comprehensive study of nucleon structure, transition form factors of baryon resonances, search for missing resonances, measurements of the spin structure of nucleons using polarized electrons on polarized hydrogen and deuterium targets, and studies of nucleon correlations inside nuclei.

3 The CLAS Detector

The CLAS design is based on a toroidal magnetic field. The primary requirements driving this choice were the ability to measure charged particles with good momentum resolution, provide geometrical coverage of charged particles to large angles in the laboratory, and keep a magnetic-field-free region around the target to allow the use of dynamically polarized targets. A view of the CLAS detector, its associated equipment, and the beamline is shown in Fig. 2.

The CLAS magnetic field is generated by six superconducting coils arranged around the beam line to produce a field pointing primarily in the ϕ-direction. A view of the particle detection system in the direction of the beam (cut in the target region) is given in Fig. 3, and normal to the beam in Fig. 4. The particle detection system consists of drift chambers [8–10] to determine the trajectories of charged particles, gas Cerenkov counters [11] for electron identification, scintillation counters [12] for measuring time of flight, and electromagnetic calorimeters [13,14] to detect showering particles (electrons and photons) and neutrons. The segments are individually instrumented to form six essentially independent magnetic spectrometers with a common target, trigger and data-acquisition system.

Some configuration adjustments are required to permit CLAS to operate with

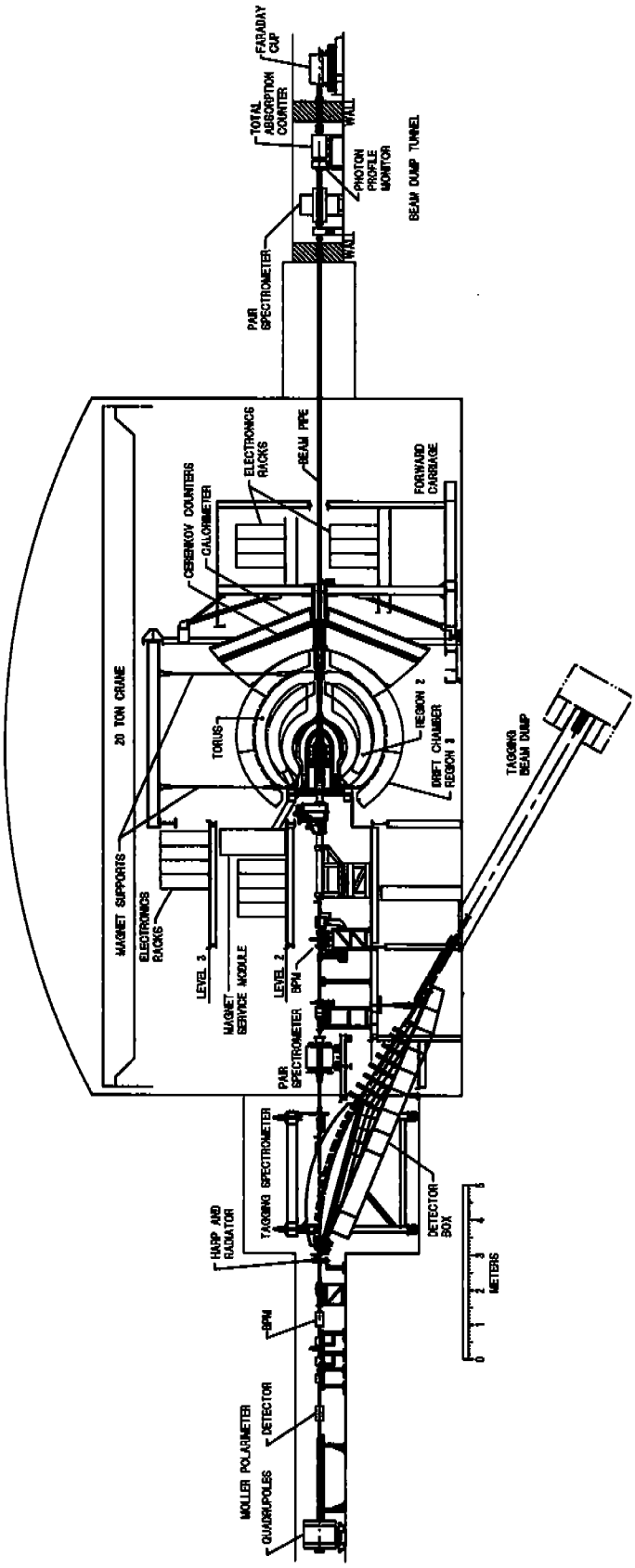

Fig. 2. Side view of the CLAS detector in Hall B with beamline and associated equipment.

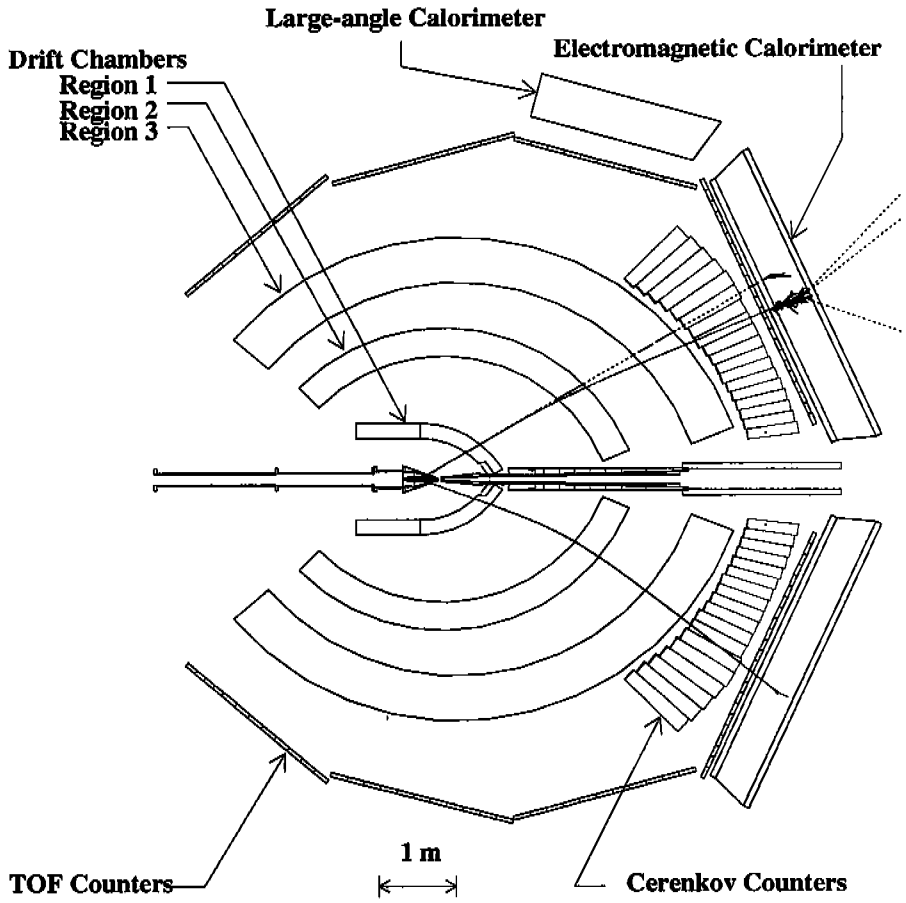

Fig. 3. A schematic top view of the CLAS detector cut along the beam line. Typical photon, electron, and proton tracks (from top to bottom) from an interaction in the target are superimposed on the figure.

either electron or photon incident beams. For electron scattering experiments, a small normal-conducting "mini-torus" surrounds the target to keep low momentum electrons produced by Møller scattering in the target from reaching the innermost drift chambers. The mini-torus coils are indicated in Fig. 4. For tagged-bremsstrahlung experiments, the mini-torus is replaced by a scintillator start-counter [15] that provides a fast input to the trigger, and identifies the correct start time for time-of-flight measurements. Further operational details for both electron and photon beams appear in the sections immediately following the description of the CLAS itself.

A two-level trigger system is used to initiate data conversion and readout. The Level-1 trigger can make use of any or all of the fast information from the time-of-flight counters, the Cerenkov counters, and the electromagnetic calorimeters. A Level-2 trigger adds crude track finding using hit patterns in the drift chambers. The data acquisition system collects the digitized data and stores the information for later off-line analysis.

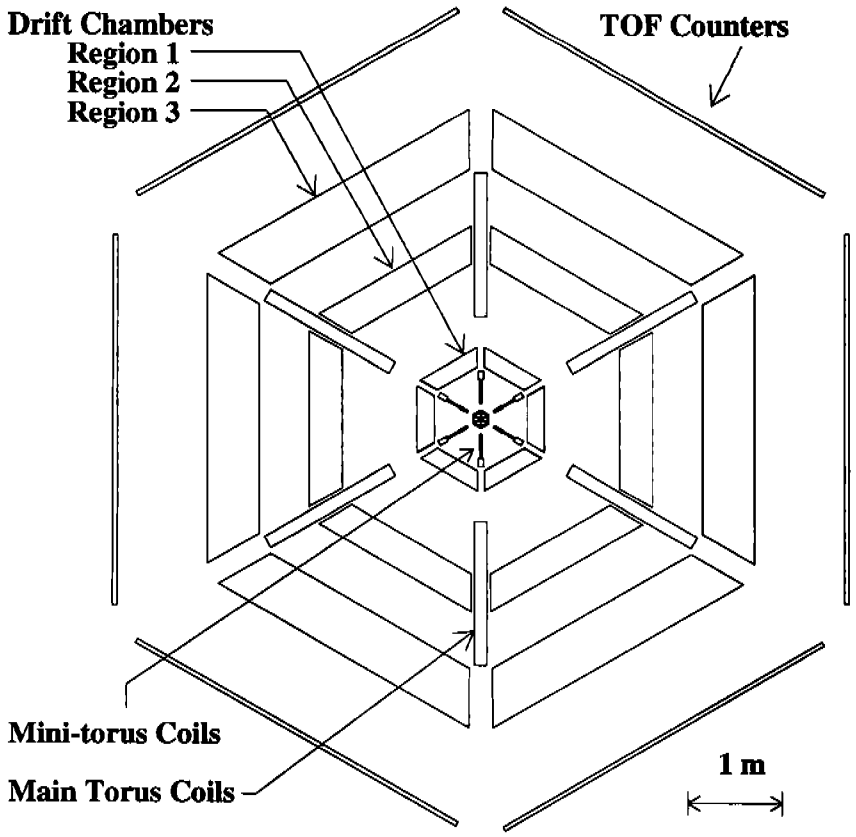

Fig. 4. Schematic view of the CLAS detector, showing a cut perpendicular to beam. Also shown is the mini-torus used only for electron runs.

In the following sections, each of the CLAS subsystems is described in more detail, with a summary of its performance in the last section. A conventional spherical coordinate system is used in all of the descriptions in this paper. The z-axis is taken to lie along the beam direction, with θ as the polar (scattering) angle, and ϕ as the azimuthal angle. The x and y directions are then, respectively, horizontal and vertical in the plane normal to the beam.

3.1 Torus Magnet

The magnetic field for the momentum analysis of charged particles is generated by six superconducting coils arranged in a toroidal geometry around the electron beam line. There is no iron in the system, so the magnetic field is calculated directly from the current in the coils. The layout of the coils and contours of constant absolute field strength are shown in Fig. 5A. The magnet is approximately 5 m in diameter and 5 m in length. Fig. 5B shows the magnetic field vectors in a plane perpendicular to the torus axis at the target

position. The main field component is in the ϕ-direction, however, there are significant deviations from a pure ϕ-field close to the coils. The effect of these deviations on the particle trajectories is minimized by the circular inner shape of the coil: particles coming from the target do not experience a significant deflection in ϕ when crossing the inner boundary of the coil.

The kidney-shape of the coils results in a high field integral for forward-going particles (typically high momentum), and a lower field integral for particles emitted at larger angles. At the same time, this coil geometry preserves a central field-free volume for the operation of a polarized target. At the maximum design current of 3860 A, the total number of amp-turns is 5×10^6 (summed over all loops). At this current the integral magnetic field reaches 2.5 Tesla·meter in the forward direction, dropping to 0.6 Tesla·meter at a scattering angle of 90°. Routine operation has been limited to 87% (3375 A) of the maximum current to keep internal mechanical stresses within conservative limits.

Based on a CEBAF reference design, Oxford Instruments Inc. finalized the design of the toroidal magnet, constructed the coils, and assembled the magnet in Hall B [16,17]. Each of the six coils has 4 layers of 54 turns of aluminum-stabilized NbTi/Cu conductor. Cooling of the coils to 4.5 K is accomplished by forcing super-critical helium through cooling tubes located at the edge of the windings. Super-insulation and an intermediate liquid-nitrogen-cooled heat shield reduce the heat load. The coils are designed to be self-protecting in case of a quench.

The individual coils are subject to strong centering forces (maximum 1.4×10^6 N) that are transmitted from the coils via three internal warm-cold support links to the coil cryostat. Out-of-plane forces, arising from gravitational loads and from magnetic forces due to asymmetries in the coil geometry, are transmitted via six pairs of short, fiberglass-epoxy compression struts per coil to the cryostats. Support rings in the front and back of CLAS determine the position of the cryostats at the inside radius. At the outer perimeter, the distance between neighboring cryostats is set by five carbon-fiber rods with 25-mm diameter.

3.2 Drift Chambers

The CLAS toroidal magnet bends charged particles toward or away from the beam axis but leaves the azimuthal angle essentially unchanged. The magnet coils naturally separate the detector into six independent tracking areas or "sectors". To simplify detector design and construction, 18 separate drift chambers were built and located at three radial positions in each of the six

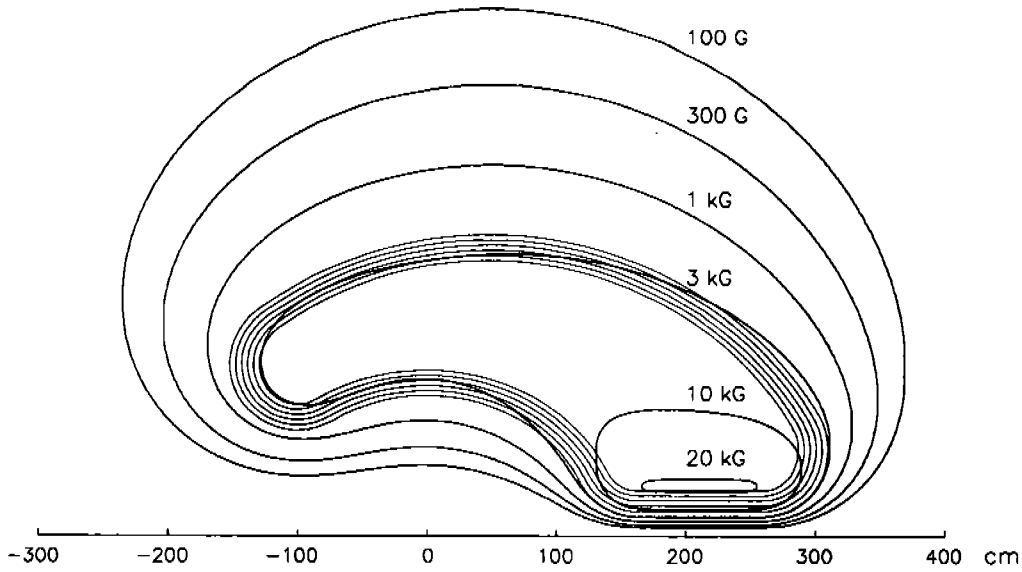

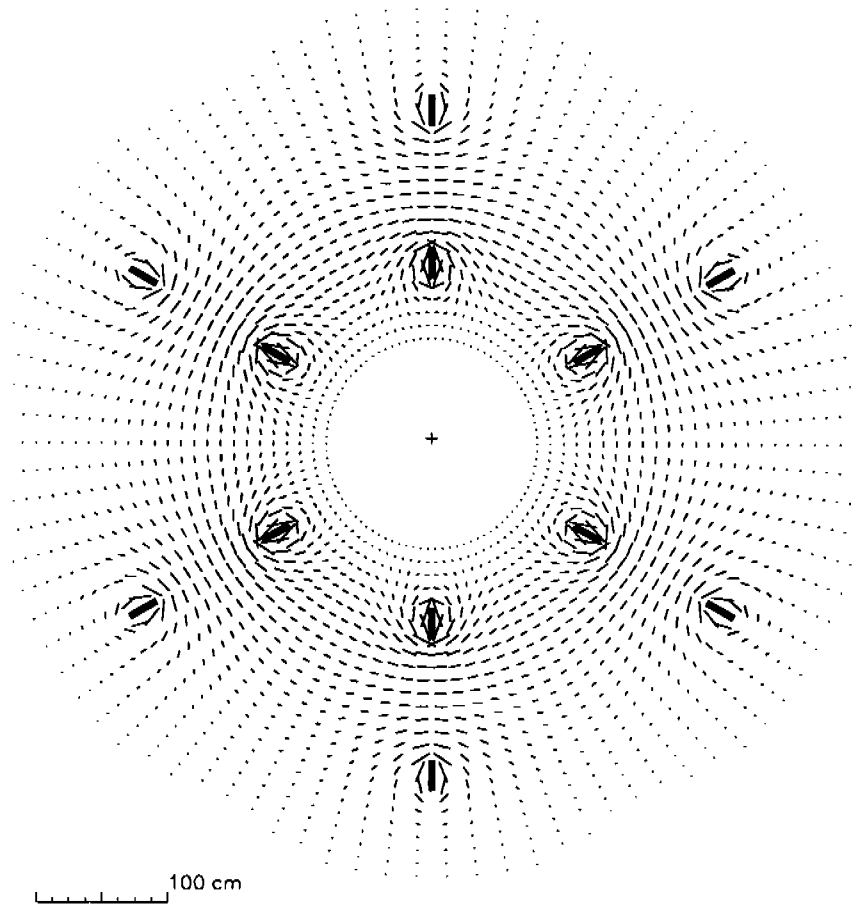

Fig. 5. A.(top) Contours of constant absolute magnetic field for the CLAS toroid in the midplane between two coils. The projection of the coils onto the midplane is shown for reference; B.(bottom) Magnetic field vectors for the CLAS toroid transverse to the beam in a plane centered on the target. The length of each line segment is proportional to the field strength at that point. The six coils are seen in cross section.

sectors. These radial locations are referred to as "Regions". The six "Region One" chambers (R1) surround the target in an area of low magnetic field, the six "Region Two" chambers (R2) are situated between the magnet coils in an area of high field near the point of maximum track sagitta, while the six "Region Three" chambers (R3) are located outside of the magnet coils. These relative positions are shown in Fig. 3 and Fig. 4. See Refs. [8–10] for more details.

To optimally fill the wedge-shaped sector volume, the chamber bodies were designed to support wires stretched between two endplates, each parallel to its neighboring coil plane, and thus tilted at 60° with respect to each other. This design provides maximum sensitivity to the track curvature since the wire direction is approximately perpendicular to the bend plane. The wire midpoints are arranged in "layers" of concentric (partial) circles, with the wire positions shifted by half the nominal wire spacing in successive layers. This pattern of wires in neighboring layers, with a repeating pattern of two field-wire layers and one sense-wire layer, results in a quasi-hexagonal pattern with six field wires surrounding one sense wire. The cell size increases uniformly with increasing radial distance from the target. The average distance between field and sense wires is 0.7 cm in R1, 1.5 cm in R2, and 2.0 cm in R3.

For pattern recognition and tracking redundancy, the wire layers in each chamber are grouped into two "superlayers" of six wire layers each, one axial to the magnetic field, and the other tilted at a 6° stereo angle to provide azimuthal information. The stereo superlayer of R1 is an exception to this rule, consisting of only four wire layers due to space constraints. A detail of the wire layout is shown in Fig. 6. The total number of sense wires in the drift chamber system is 35,148.

All six inner R1 chambers were assembled into a single self-supporting structure and inserted into the CLAS torus. The R2 chambers are located between the coil cryostats. To achieve accuracy of placement as well as protection from stresses due to cryostat motion, one endplate of each sector is rigidly attached to the cryostat and the other endplate is spring-mounted to the neighboring cryostat. After installation, the wire tension is transfered from a temporary frame to the cryostats. Each of the six R3 chambers was designed as an individual, self-supporting rigid structure that bears the wire tensions internally. Each R3 chamber was installed by attaching it to the outside edges of the cryostats as shown in Fig. 7. See Refs. [8–10] for more details on the design and construction of the chambers.

From considerations of system safety, as well as to improve the operating lifetime, an 88% - 12% mixture of argon and CO_2 was selected. An active feedback system maintains constant pressure at the chamber regardless of atmospheric fluctuations by making small adjustments to the out-flow. The

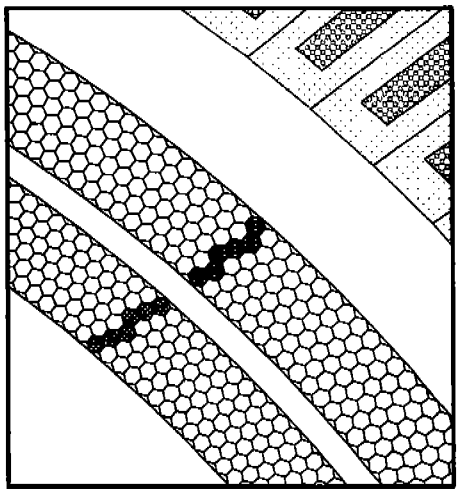

Fig. 6. Representation of a portion of an R3 chamber, showing the layout of its two superlayers. The sense wires are at the center of each hexagon and the field wires are at the vertices. There is no material at the perimeters of the hexagonal cells, but these are shown to outline the regular layout of the wires. Not shown are the guard wires that surround each superlayer. In this view, projected onto the mid-plane of the sector, a passing charged particle is shown by the highlighted drift cells that have fired. Beyond the drift chamber, in the upper right corner, the edges of several Cerenkov modules are visible.

average flow-rate for the R1, R2, and R3 chambers is 5.5, 26, and 45 liters per minutes, respectively. This corresponds to 5, 3, and 1.5 volume exchanges per day.

A high-voltage system maintains the sense-wires at a positive potential and the field wires at a negative potential whose absolute value is half that of the sense-wires. A layer of guard wires surrounds the perimeter of each superlayer, with the high-voltage potential adjusted to approximate the electric-field configuration of an infinite grid. This three-voltage scheme minimizes the effects of nearby grounded surfaces such as the endplate.

Each sense wire is instrumented with a single-channel differential pre-amplifier typically mounted in groups of 48 on a printed circuit board which is attached to the chamber endplate. The outputs of each group of 16 pre-amps are carried via a 17-pair, twisted-pair cable to a crate-mounted post-amplifier and discriminator board (ADB) that produces digital output pulses. The ADB output pulses form the input to a multi-hit, common-stop TDC board.

During system commissioning, the values for the discriminator thresholds in the ADBs were set to keep the electronic-noise contribution to the hit-wire occupancy below the 2% level. The high-voltage settings were determined from a plateau run, resulting in individual "layer efficiencies" –the probability that a good hit is recorded in a wire layer through which a charged particle has passed– of greater than 98%.

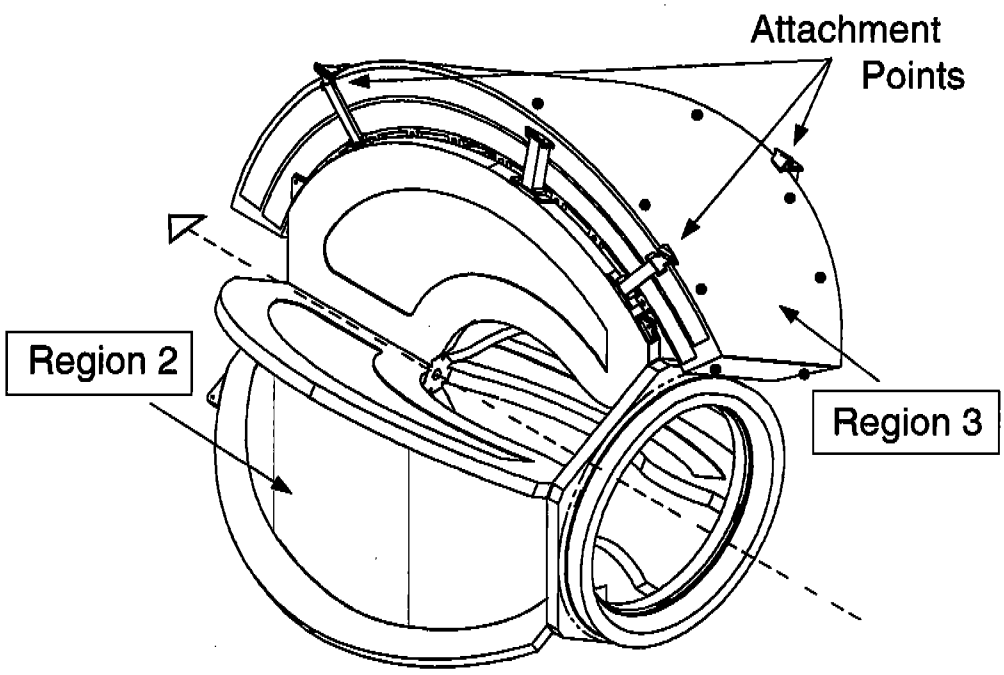

Fig. 7. An R2 chamber (lower left) and an R3 chamber (upper right) shown in their installed positions on the torus cryostat. The R1 chambers are not shown. For the R3 chamber the three attachment points are indicated.

The tracking resolution is the deviation of the reconstructed momenta and angles of the charged-particle tracks from their true values at the interaction vertex. Tracking uncertainties arise from multiple scattering in the material along the particle trajectory, from geometric misalignments of the separate chambers, from lack of knowledge of the true value of the traversed magnetic field strength, and from the single-wire resolution. The single-wire resolution depends upon where within a cell the track has passed. Within a given layer, this is estimated by fitting a track to all hits except those in that layer. The fit residual is the difference between the fitted distance-of-closest-approach (DOCA) of the track and the DOCA value calculated from the drift time in the excluded layer.

Figure 8 shows the rms width of the track-hit residual distribution plotted versus DOCA for Region 2. The single-wire resolution worsens near the wire and also at the outer edge of the cell. This arises due to the Poisson distribution of ion-pair production along the path of the primary ion near the sense wire, along with time-walk effects and the divergence of the electric field lines near the field wire. The average single-wire resolution in the mid-portion of the cell for each region is about 200 to 250 μm. The whole-cell average is about 310, 315, and 380 μm for R1, R2, and R3, respectively. For a summary of the overall track momentum and angular resolutions achieved with these spatial

resolutions, see the section on detector performance.

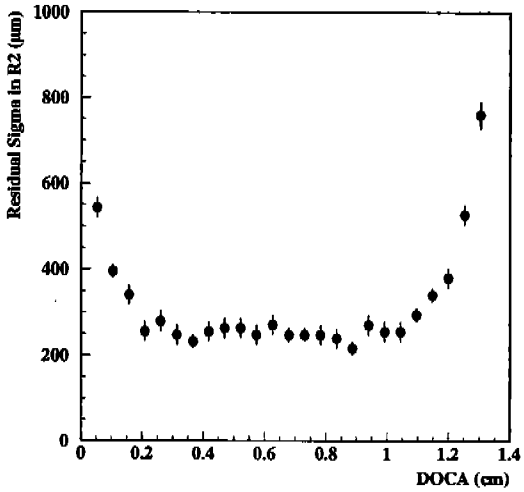

Fig. 8. Track-hit residual rms width as a function of the fitted DOCA for Region 2 chambers.

3.3 Cerenkov Counters

The Cerenkov Counter (CC) [11] serves the dual function of triggering on electrons and separating electrons from pions. The design of the Cerenkov detector aims at maximizing the solid-angle coverage in each of the six sectors out to an angle $\theta = 45°$ with the least possible amount of material (to prevent degradation of the energy resolution). This is achieved by placing the light collecting cones and photomultiplier tubes (PMTs) in the regions of ϕ that are already obscured by the magnet coils, and covering as much of the available space as possible with mirrors (see Fig. 9). Since charged-particle trajectories

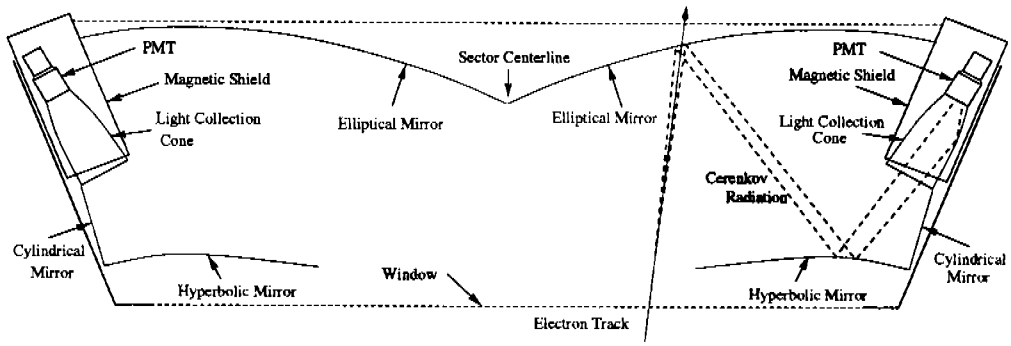

Fig. 9. Schematic diagram of one Cerenkov segment, symmetric about the sector center. Also shown is an example of an electron trajectory with the collection of Cerenkov light to the PMT. The PMTs, magnetic shields, and light-collecting Winston cones, lie in the region of the detector obscured by the CLAS magnet coils, and thus do not affect the electron acceptance.

lie approximately in planes of constant ϕ, the placement of the PMTs in the

shadows of the magnet coils does not affect the angular coverage. The light collection optics was designed to focus the light only in the ϕ direction, which preserves information on the electron polar angle θ_e. The full θ range of each of the six sectors was divided into 18 regions, as may be seen in Fig. 3, and each θ segment was divided into two modules about the symmetry plane bisecting each sector. This results in a total of 12 identical (except for an inversion symmetry) subsectors around the ϕ direction for each θ interval, and a total of 216 light-collection modules.

The PMTs employed for the Cerenkov detectors are 5-inch Phillips model XP4500B's. The PMTs are equipped with high-permeability magnetic shields, since they are located in the fringe field region of the torus, with the highest transverse fields reaching 70 G at large scattering angles. The optical elements of each module include one elliptical and one hyperbolic mirror to provide the primary focusing, a cylindrical mirror used to compensate for imperfections in the focusing, and a light collection (Winston) cone.

The Cerenkov radiator gas used in the detector is perfluorobutane (C_4F_{10}) which has an index of refraction of 1.00153. This results in a high photon yield and a pion momentum threshold of 2.5 GeV/c. This gas also has excellent transmission properties for light at short wavelengths. Each sector of the detector holds approximately six cubic meters of gas. The recirculating gas system maintains constant pressure in the gas volume, and removes impurities from the gas.

The single-photoelectron response of the photomultiplier is used to equalize the gain of the PMTs, and to calibrate the response of the detector in terms of the number of photoelectrons. An inbending electron, traversing the active volume of the detector, results in typically 4–5 photoelectrons.

3.4 Time-of-Flight Counters

The time-of-flight (TOF) counters [12] cover the polar angular range between 8° and 142° and the entire active range in azimuthal angle ϕ. The scintillators are located radially outside the tracking system and the Cerenkov counters but in front of the calorimeters. Their alignment and relative positioning with respect to other detector subsystems is most clearly seen in Fig. 3. The scintillator thickness of 5.08 cm is uniform throughout, chosen to give a large signal for traversing minimum-ionizing particles. Each scintillator is positioned such that it is perpendicular to the average local particle trajectory. The width of each counter subtends about 1.5° of scattering angle. The forward counters (at θ less than 45°) are 15-cm wide, and the large-angle counters are 22-cm wide, in the $\Delta\theta$ direction.

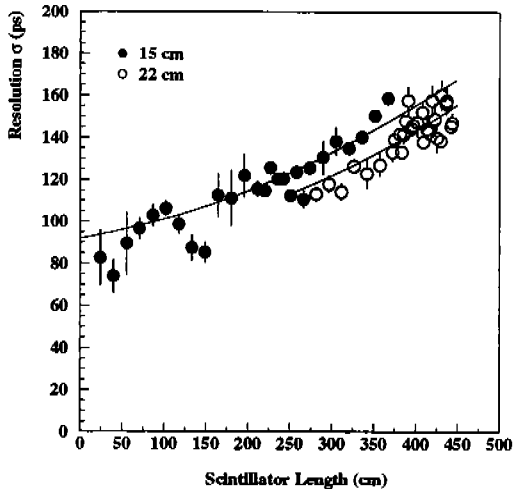

Fig. 10. Time resolution of the TOF counters determined by cosmic-rays for the 15-cm wide (filled circles) and the 22-cm wide (open circles) counters. The lines are the results of the parameterization described in the text.

Each TOF counter consists of Bicron BC-408 scintillator with a PMT at each end. The forward-angle and large-angle counters were instrumented with Thorn EMI 9954A and Philips 4312B/D2 PMTs, respectively.

The principal features of the TOF system can be described by the following simplifications: The attenuation length of the forward-angle counters, which are 32 to 376 cm in length, can be approximated by λ = 134 cm + 0.36·L, and the propagation velocity by v_{eff}= 15 cm/ns + 0.0033·L/ns, where L is the length of the counter in cm. The large-angle scintillators, 371 to 445 cm in length, have an approximate attenuation length of 430 cm, and a corresponding constant v_{eff}= 16.5 cm/ns. The time resolution of each counter has been measured with cosmic-rays (Fig. 10); it can be parameterized with the following formula:

$$\sigma_{TOF}(\mathrm{ns}) = \sqrt{\sigma_0^2 + \frac{\sigma_1^2 + (\sigma_P \cdot L/2)^2}{N_{pe} \cdot \exp(-L/2\lambda)}}\,, \tag{1}$$

where σ_0=0.062 ns represents the intrinsic resolution of the electronic measuring systems and other processes that are independent of light level, σ_1 = 2.1 ns is the combined single-photoelectron response of the scintillator and PMT, and σ_P = 0.0118 ns/cm accounts for path-length variations in the light collection. Path-length variations in the scintillator scale with the distance from the source to the PMT, which on average is half the length of the counter ($L/2$). The statistical behavior of the last two terms is indicated by scaling the single-photoelectron responses by $\sqrt{N_{pe}}$, where N_{pe} = 1043 is the average number of photoelectrons that would be seen by the PMT of a hypothetical counter without attenuation. For scintillators that are several meters in

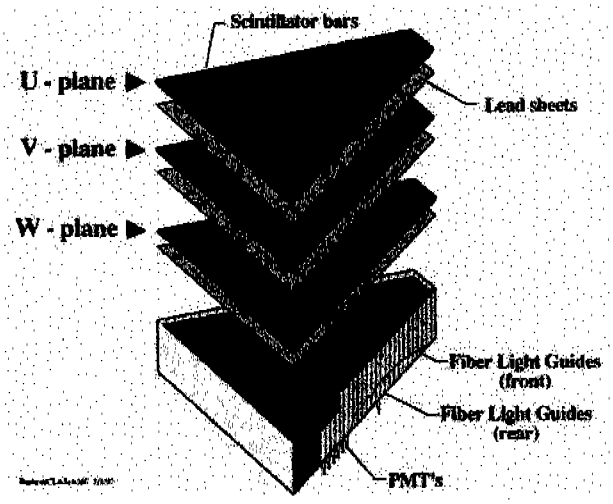

Fig. 11. Exploded view of one of the six CLAS electromagnetic calorimeter modules.

length, the dominant contribution to the timing resolution comes from transit time variations of photon paths in the scintillator. The parameterization of the TOF resolution is shown in Fig. 10.

3.5 Forward Electromagnetic Calorimeter

3.5.1 Design

The main functions of the forward electromagnetic calorimeter (EC) are detection of and triggering on electrons at energies above 0.5 GeV, detection of photons at energies above 0.2 GeV (for reconstructing π^0 and η via the measurement of their 2γ decays), and detection of neutrons. This detector covers the θ range up to 45°. Based on the requirements of energy and position resolution over a large area, a sampling calorimeter made of alternating layers of scintillator strips and lead sheets with a total thickness of 16 radiation lengths was chosen. A lead-scintillator thickness ratio of 0.24 was used, requiring total thicknesses of 39 cm of scintillator and 8.4 cm of lead. For a complete description of the forward electromagnetic calorimeter see Ref. [13].

For each EC module, the lead-scintillator sandwich is contained within a volume having the shape of a nearly equilateral triangle. There are 39 layers in the sandwich, each consisting of a 10-mm thick scintillator followed by a 2.2-mm thick lead sheet. The calorimeter utilizes a "projective" geometry pointing to the nominal target position, i.e. the area of each successive layer increases linearly with distance. For readout purposes, each scintillator layer consists of 36 strips parallel to one side of the triangle, with the orientation of the strips rotated by 120° in successive layers (Fig. 11). Thus there are three orientations, or views (labeled U, V, and W), each containing 13 layers, which provide

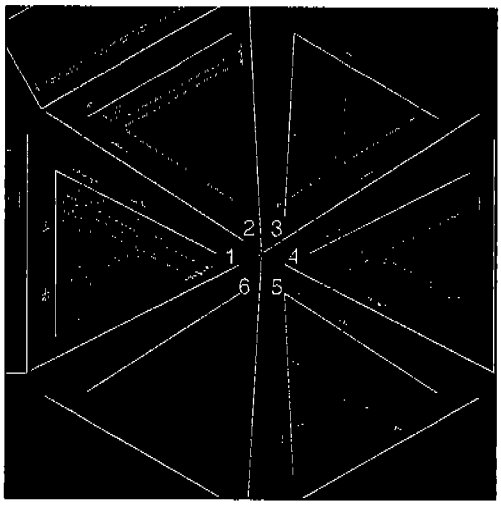

Fig. 12. Event reconstruction in the electromagnetic calorimeter. In sectors 2, 3, 4, and 5, a single intersection of peaks on each view (U, V, W) is found, while in sector 1, two hits are reconstructed. The size of the oval at each intersection depicts the transverse energy spread in the shower.

stereo information on the location of the energy deposition. Each view is further subdivided into an inner (5 layers) and outer (8 layers) stack, to provide longitudinal sampling of the shower for improved electron/hadron separation. The readout is accomplished using 1296 XP2262 PMTs. To monitor the gain stability, a nitrogen-laser calibration system is used to excite a reference scintillator, whose light is injected into each PMT via quartz fibers.

3.5.2 Hit reconstruction

To reconstruct a hit in the EC, energy deposition is required in all three views (U,V,W) of the inner or outer layers of a module. The algorithm first identifies groups of strips in each of the three views. Neighboring strips are placed in groups if their PMT signals are above a software threshold, and the position centroid and root-mean-square for each group are calculated. After all groups are found, the intersection points of different groups from each view are reconstructed. Each intersection corresponds to a hit. The energy and the time of the hit are then calculated by taking into account the path lengths from the hit position to the readout edge. The energy of a single peak may be assigned to more than one hit using appropriate weighting when multiple hits overlap in a single view. In Fig. 12 an event is shown with hits reconstructed in five EC modules, including two hits in sector 1.

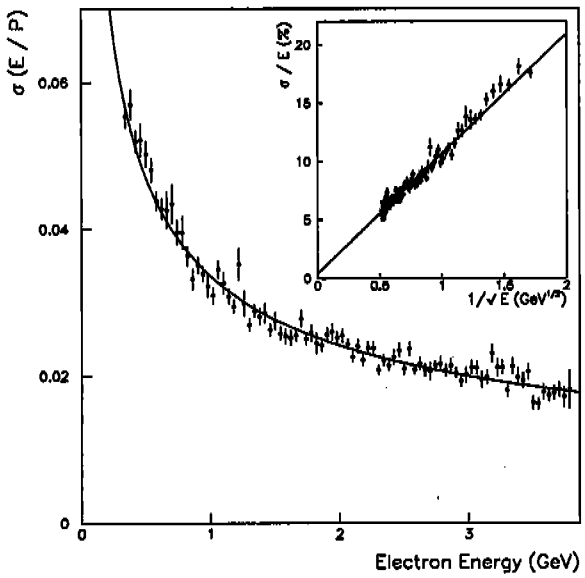

Fig. 13. Variation of the energy deposited in the active scintillator of the EC normalized to incident electron momentum. The inset shows the linear dependence of $\sigma(E)/E$ on $E^{-1/2}$, where the fitted line yields a stochastic resolution of $10.3\%/\sqrt{E}$.

3.5.3 Performance

A fiducial region for the forward calorimeter has been defined that excludes hits within 10 cm of the edge of the module to ensure that the shower is fully contained within the detection volume. All results quoted below include this condition.

The energy resolution of the forward calorimeter for electrons is shown in Fig. 13; it can be parameterized as:

$$\frac{\sigma}{E} = \frac{10.3\%}{\sqrt{E(GeV)}}, \tag{2}$$

with a negligible constant term. The sampling fraction is approximately 0.3 for electrons of 3 GeV and greater, and for smaller energies, there is a monotonic decrease to about 0.25 for electrons of 0.5 GeV. The average rms position resolution is 2.3 cm for electron showers with more than 0.5 GeV of energy deposited in the scintillator. The timing resolution for electrons averages 200 ps over the entire detector.

The Large Angle Calorimeter (LAC) provides detection of scattered electrons and neutral particles such as neutrons and photons coming from radiative processes or from the decays of π^0 and η mesons. The LAC covers only two of the six CLAS azimuthal sectors (corresponding to 120° in ϕ) and a range of the scattering angle θ between 45° and 75°.

The LAC is a sampling calorimeter composed of two identical modules with a multi-layer structure of lead sheets and scintillator bars similar to the forward calorimeter. A single LAC module consists of 33 layers, each composed of a 0.20-cm thick lead foil and 1.5-cm thick NE110A plastic scintillator bar [18]. The geometry is projective with scintillators of 10-cm average width. Each LAC module corresponds to 12.9 radiation lengths and 1.0 hadronic absorption lengths. To avoid optical coupling, 0.2-mm thick Teflon sheets separate neighboring scintillators. Scintillator bars in consecutive layers are rotated by

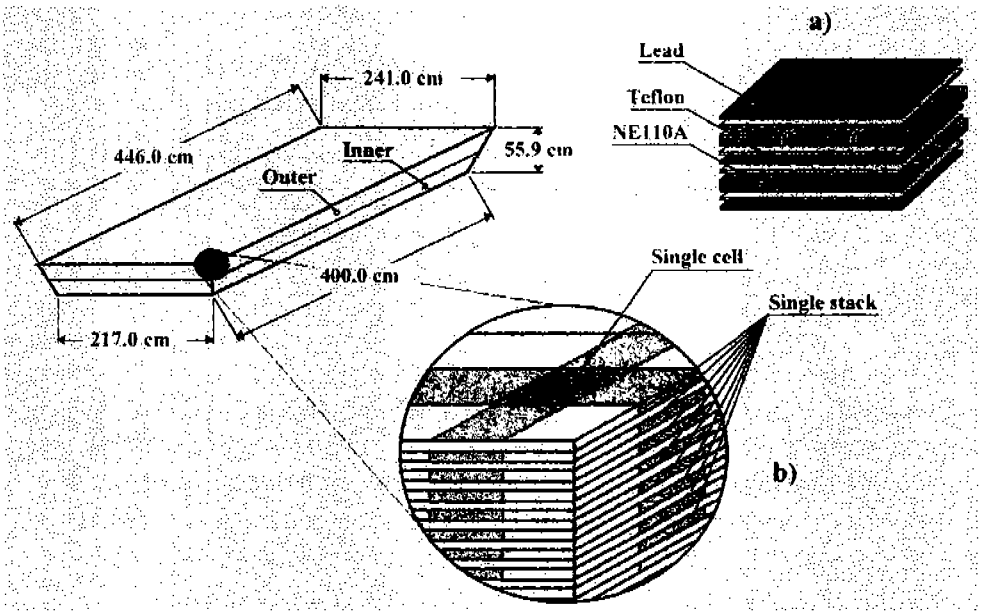

Fig. 14. Tapered geometry of one LAC module and a schematic view of the lead-scintillator sandwich structure with details of a) the calorimeter layers and b) the composition of a stack of scintillators that are read out together.

90° to form a 40 × 24 matrix of roughly 10 × 10 cm^2 cells (see Fig. 14). To improve the e^-/π^- discrimination, the LAC modules are longitudinally divided into inner (17 layers) and outer (16 layers) regions with individual light readouts.

The light produced by the showers in the active material is collected at both scintillator ends by Lucite light guides coupled to each bar via an air gap [19]. The light guides form a stack that couples to EMI 9954A photomultipliers, and

each module is equipped with 256 PMTs [20]. The gain stability of each LAC photomultiplier is monitored with a precision of $\leq 0.5\%$ using a radioactive source of α-particles (^{241}Am) sealed within a YAP scintillator crystal [21].

3.6.1 Performance

The LAC energy resolution for electromagnetic showers [18,22] can be parameterized as:

$$\frac{\sigma(E)}{E} = \frac{(7.5 \pm 0.2)\%}{\sqrt{E(\mathrm{GeV})}}. \tag{3}$$

The π^- contamination is less than 1% [23] for cuts that give a detection efficiency of 95% for 2 GeV electrons. A quantitative check of the LAC equalization and energy calibration can be obtained by reconstructing the π^0 invariant mass from 2-γ events.

Good timing resolution for the LAC is essential to determine the momentum of neutrons via time-of-flight. For neutron detection efficiencies greater than 30%, we obtained a time resolution of 260 ps [23] for momenta higher than 0.5 GeV/c. Neutrons are separated from photons by requiring $\beta_{neutral} \leq 0.95$.

3.7 Detector Electronics

Many of the detector subsystems use the same type of electronic modules for readout. This minimizes the complexity of the system, simplifies initial integration, and eases the requirements for maintenance. The general philosophy was to acquire commercial electronics modules whenever possible, and to develop custom electronics only when commercial options were not available, or the application was so specialized that significant gains in performance or cost could be achieved by an in-house design. Initially, all analog signals were digitized using commercial FASTBUS modules. Recently, however, as new detectors are being added, more electronic modules are available in VME, and are being integrated into the system.

The wire signals from the drift chamber system are read out using LeCroy 1877 pipeline time-to-digital converters (TDCs) with a least count of 0.5 ns. These are operated in common stop mode to eliminate the need for signal delay cables. The multi-hit capability of the modules is used to multiplex the timing information of two wires into a single TDC channel, thereby reducing by a factor of two the number of FASTBUS modules needed. Details of this setup can be found in Ref. [8]. The multiplexing is accomplished using a custom

amplifier and discriminator board that receives information from pairs of wires, discriminates the signals, and outputs two different standard pulse widths. The hit wire is identified using the feature of the TDC that records both leading and trailing edges of each input pulse to determine the pulse width.

For the PMT-based detectors, the signal times are digitized using LeCroy FASTBUS 1872A TDCs, and the pulse heights are converted using LeCroy FASTBUS 1881M analog-to-digital converters (ADCs). Most TDCs are fed from leading-edge LeCroy 2313 CAMAC discriminators set at a low threshold, typically 20 mV. The large angle calorimeter time measurements were accomplished using LeCroy 1875A FASTBUS modules fed by CAEN C207 CAMAC discriminators. The high-resolution TDCs, set to a nominal least count of 50 ps, are needed to achieve the required timing resolution for time-of-flight measurements. The ADC information is used to determine the energy deposition in each detector, as well as to correct to the TDC measurements for time walk.

The inputs to the Level 1 trigger are generated using custom electronics to sum appropriate groupings of PMT signals that can be used to generate fast signals with high efficiency. Electron-beam experiments require energy deposition in the calorimeter, as well as a signal above threshold in the Cerenkov counter. Photon-beam experiments require a coincidence between the tagging spectrometer, the start counter, and a hit in the time-of-flight system. In order to study the trigger in software, these inputs are also recorded in the data stream with LeCroy 1877 FASTBUS pipeline TDCs along with all other trigger inputs.

High voltage was provided to each PMT using LeCroy 1450 mainframes with 1461N (negative) cards for the calorimeter and the TOF counters, and 1461P (positive) cards for the Cerenkov PMTs. The drift chamber system high voltage was delivered using the CAEN 527 system, which was also used to provide high voltage to the large angle calorimeter PMTs.

3.8 Trigger System

To acquire events of interest while minimizing the deadtime, a two-level hierarchical trigger system was designed [24]. The Level 1 trigger is deadtimeless, processing all prompt PMT signals through a pipelined memory lookup within 90 ns. The resulting signals are sent to a trigger supervisor module (see Sec. 3.8.3), where they are used to gate the front-end electronics. This includes generating the common start signal for the PMT TDCs, the integrating gate signal for the PMT ADCs and, with some delay added, the common stop signal for the drift chamber TDCs.

After the Level 1 trigger signal has occurred, the event is digitized and read out, unless a fast-clear signal is issued within a period of time called the fast-clear window. The fast-clear window is set to the sum of the longest possible drift time in the drift chambers plus the time required for the Level 2 processing ($\sim 4\ \mu s$). The Level 2 trigger is designed to make use of this fast-clear capability by clearing events that satisfied Level 1, but which have no tracks in the drift chambers. It does this by finding "probable tracks" in the detector, and issuing a fast-clear if no track candidates are found (see Section 3.8.2). The detector cannot accept any more triggers until either a fast clear occurs or digitization is completed. The event readout proceeds asynchronously with digitization, and does not contribute to the system deadtime.

3.8.1 Level 1

The underlying idea of the Level 1 trigger [25,26] is to allow the use of any or all available prompt information from the PMT channels to determine if a desired event has occurred. This information includes the general location of hits in the TOF detector, the signals in the Cerenkov detector (for electron identification), and the energy deposited in the calorimeter. Bit patterns from these detector subsystems are compared against patterns preloaded in memory tables for rapid response. The system involves a three-stage pipelined memory lookup with a pipeline speed of 67 MHz. These bit-consolidation stages are indicated schematically in Figs. 15 and 16.

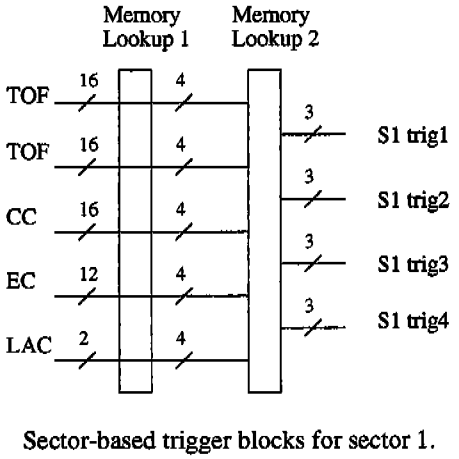

Fig. 15. Schematic diagram of the generation of four sector-based "trigger blocks" from the information in a single sector. Each block contains three trigger definitions.

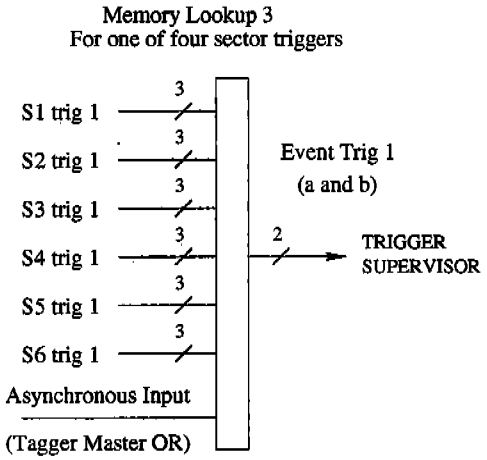

Fig. 16. Schematic diagram of the trigger electronics that combines information from a single block across all six sectors with the asynchronous input to produce an event trigger.

The first stage starts with 62 bits of trigger data (plus spares) from each sector. These bits indicate such things as hits in various coarse angle bins in the

TOF array and/or (within upper and lower thresholds) in the CC. They also indicate hits over some threshold setting for the total energy deposition in the EC, and whether calorimeter energy deposition was concentrated in either the inner or the outer layers. For electron runs, the total energy serves to require a minimum Q^2 in the event selection, and a relatively high energy deposition in the inner layers can serve to suppress pion triggers. Two consecutive memory lookup stages, taking two clock cycles total, serve to reduce these 62 bits to four groups of 3 that signify the likelihood of some particle(s) in this sector that are of interest to one of several possible preloaded trigger definitions.

The third lookup stage then correlates the patterns from the individual sectors in order to apply geometrical constraints on multi-pronged events. This allows such conditions as requiring that an electron in one sector be accompanied by a positive particle in the sector directly opposite, or perhaps vetoing some type of signal from the immediately adjacent sectors, etc. Additional asynchronous bits are included in the input at this stage, primarily used during photon running to correlate timing information between the photon tagger and CLAS. This third stage requires two additional clock cycles. The average processing latency of the Level 1 trigger is 90.5 ns including all propagation delays and signal processing.

The memory tables are programmed using a graphical software package called TIGRIS [27]. This allows a user to graphically define a multi-pronged trigger relative to one sector, and then automatically generate rotated configurations in other sectors to build a fully ϕ-symmetric trigger. The resulting definitions are stored as ASCII files that are converted to memory images and downloaded into appropriate hardware memory modules to allow rapid reset of trigger conditions during data collection.

3.8.2 Level 2

The Level 1 trigger can be set by events such as cosmic rays that lack matching particle trajectories in the drift chamber system. In order to reject triggers arising from these events, Level 2 [28,29] finds "likely tracks" in each sector, optionally performs a correlation with the Level 1 trigger, and generates a "Level 2 fail" signal if no correlated tracks are found. The Level 2 processing time contributes directly to the deadtime of the detector, and our goal was to make this as fast as possible, consistent with accurately finding tracks.

Identifying "likely tracks" begins by finding track segments in five superlayers in each sector (the Region 1 stereo superlayer is not used). A "segment finder" board continuously searches for track segments in overlapping regions of 16 wires $\times$ 6 layers. Track segments are found by comparing drift chamber hits with nine templates that were designed to catch all tracks passing through a

superlayer at angles of up to 60°. The segment finders may be programmed to allow up to two (out of six) layers to be missing from the template comparison, and locate the segment within the superlayer with a granularity of two cells. All template matching is done in parallel using field programmable gate arrays (FPGAs), as described in more detail in Ref. [28]. In the present implementation, a "likely track" in a sector is tagged when track segments are found in three of the five superlayers. The Level 2 trigger is satisfied by either the simple logic "OR" of these six sector tracks, or by requiring additional correlations between these tracks and the information from Level 1.

3.8.3 Trigger Supervisor

The Trigger Supervisor (TS) [30] is a custom electronics board that takes the Level 1 and Level 2 inputs from the trigger system and produces all common signals, busy gates, and resets required by the detector electronics. There are 12 trigger inputs, the first eight are used for the Level 1 triggers which may be prescaled. The other four inputs are used by various calibration triggers. There is also an input for Level 2 trigger confirmation. The TS may be programmed to require only a Level 1 input (CLASS 1) or to require both a Level 1 input and a Level 2 confirmation (CLASS 2). In a CLASS 1 trigger the TS generates the gates upon receipt of any Level 1 input, waits for conversion of all crates to complete, and then places the event on a readout queue to initiate readout. The readout occurs asynchronously with conversion. In a CLASS 2 trigger, the TS also generates the gates on a Level 1 input, but then waits a preset amount of time ($\sim$ 3.2 μs) for a Level 2 confirmation. If Level 2 fails, the TS sends a fast clear to all the front-end electronics, which causes them to reset and become active again ($\sim$ 1 μs). If the Level 2 is satisfied, the front-end modules will be allowed to convert, and the event will be placed on the readout queue for asynchronous readout.

3.9 Data Acquisition

The CLAS data acquisition (DAQ) system was designed for an event rate of 2 kHz. During the period of CLAS commissioning in 1997 the actual rate was 400 Hz. Continued development of the DAQ over five years resulted in routine operation at event rates between 3 and 4 kHz for the 2000/01 running period. The history of event acquisition rates and accumulated events for various run periods can be seen in Fig. 17. At present, the limit for the total data output rate is 25 MByte/s, constrained not by experimental hardware, but by the current use of the UNIX file system.

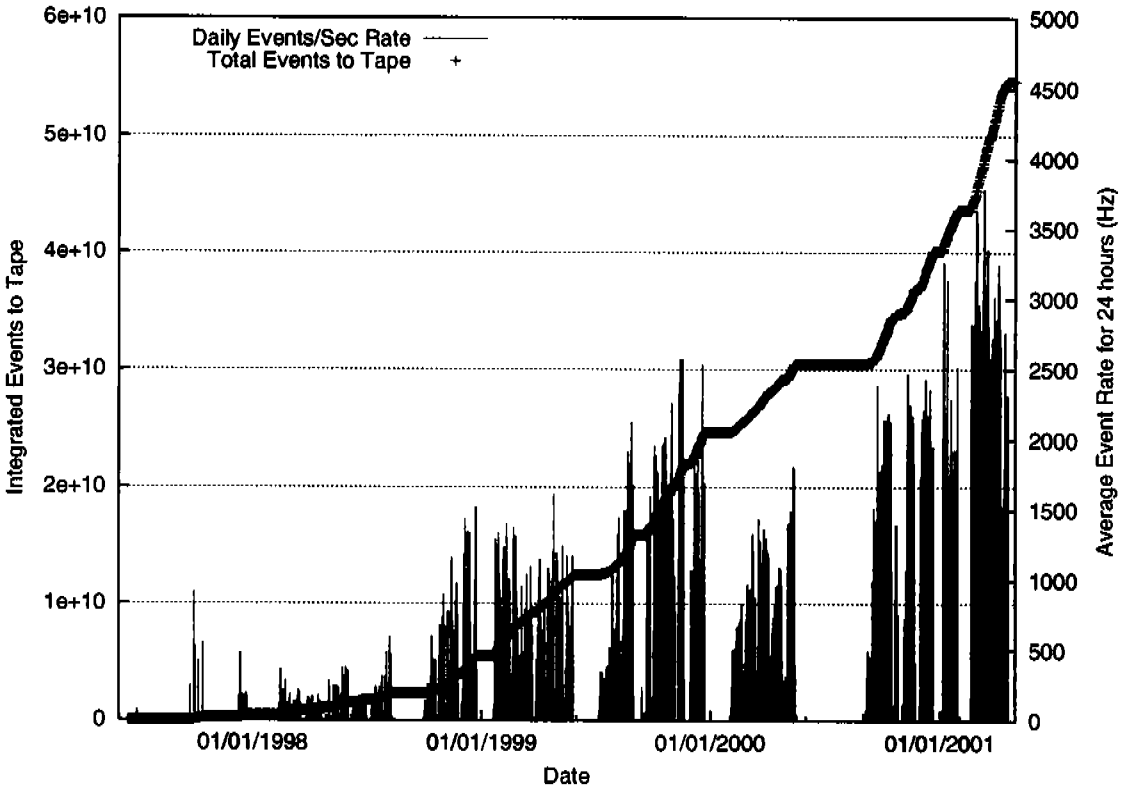

Fig. 17. Event rate and integrated events accumulated by the CLAS data system vs. time for a three year period.

3.9.1 CLAS Data Flow

The data flow is illustrated in Fig. 18. The data from the various detector components are digitized in 24 FASTBUS and VME crates within the experimental hall and collected by the 24 VME Readout Controllers (ROC1 to ROC24) in these crates. The arrays of digitized values associated with the electronic modules are then translated into tables in which each data value (up to 16 bits) is associated with a unique identity number describing the active component within the detector.

These data arrays, or event fragments, are buffered and then transfered via fast Ethernet lines to the CLAS online acquisition computer (CLON10) in the control room. Three primary processes, the Event Builder (EB), Event Transport (ET), and Event Recorder (ER), comprise the main data-flow elements in the acquisition computer. The EB on CLON10 assembles the incoming fragments into complete events. The individual tables are prefixed by headers to form "banks" that contain alphanumeric names that can be linked together. For some detectors, such as drift chambers, the electronics require several crates. Therefore, the EB combines some crate fragments into larger tables and banks. The completed event is then labeled by a run and event number, an event type, and the trigger bits that are all contained in a header bank. At

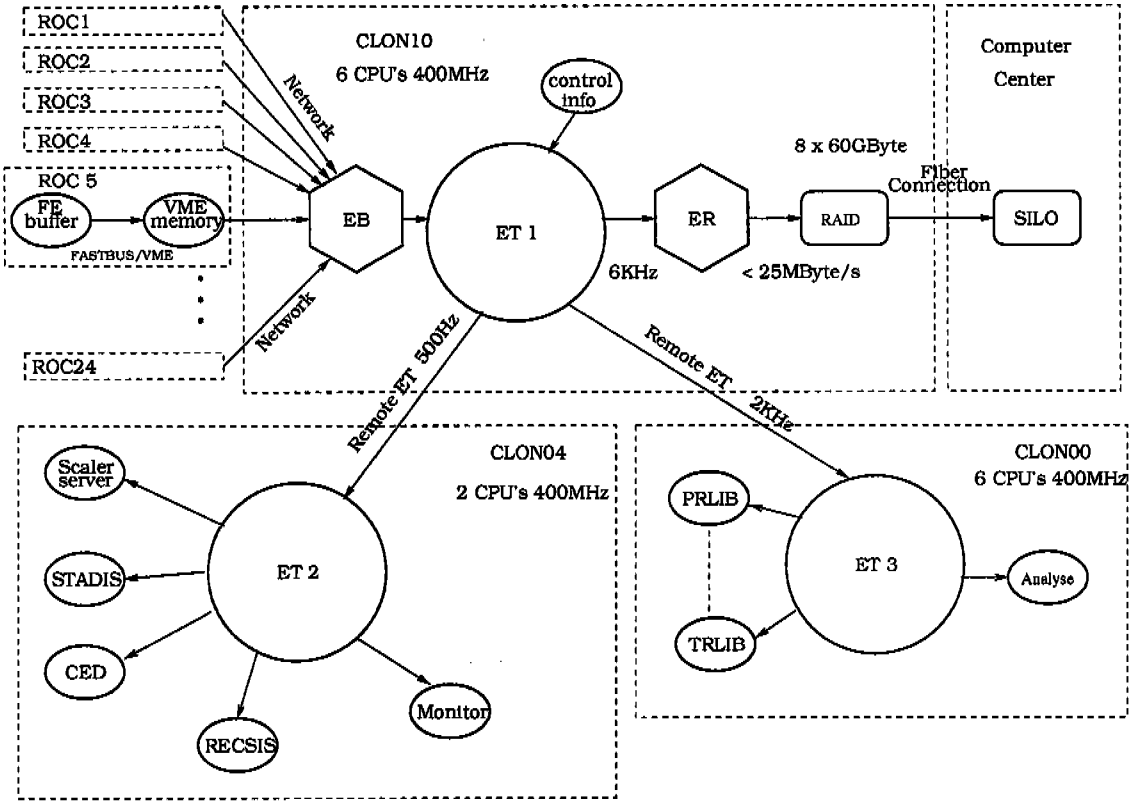

Fig. 18. Data flow schematic for CLAS, with the primary stream using the ET1 shared memory. Also shown are a variety of monitoring processes accessing data on other shared memory (ET2, ET3) managed by the ET system.

this stage the event has the final format it needs for off-line analysis.

The EB passes the completed events to shared memory (ET1) on the CLAS online computer. The ET system manages this shared memory, allowing access by various event producer and consumer processes on the same or remote processor systems. The ER picks up all events for permanent storage. Some events are transferred to remote ET systems, e.g. ET2 and ET3, for raw data checks such as hit maps, status, and event displays, and for online reconstruction, analysis, and monitoring.

The ER writes the data in a single stream to magnetic media. The output files are striped across an array of local RAID disks. A second fiber link, from the local RAID in the control room to the computer center a kilometer away, transfers the data files to the remote tape silo. Since the maximum tape writing speed at present is 10 MByte/s, data transfers are started in parallel, and successive files may end up on different tapes.

3.9.2 *Run Control Structure*

The CLAS data flow requires communication among some 100 processes running on a system of processors distributed around the detector in the experimental hall and linked to two Symmetric Multi-Processor (SMP) machines and a number of workstations in the control room. The framework for this organization is the CEBAF Online Data Acquisition (CODA) system [31]. The run control structure in Fig. 19 illustrates the sequence of setting up and performing data runs, where a single run typically lasts for one or two hours. The various processes along the horizontal axis in Fig. 19 represent the state transition for 'configuring' the set of DAQ components involved, 'downloading' executable code and parameters into the hardware components, and finally the 'prestart', 'go', and 'end' cycle for individual runs.

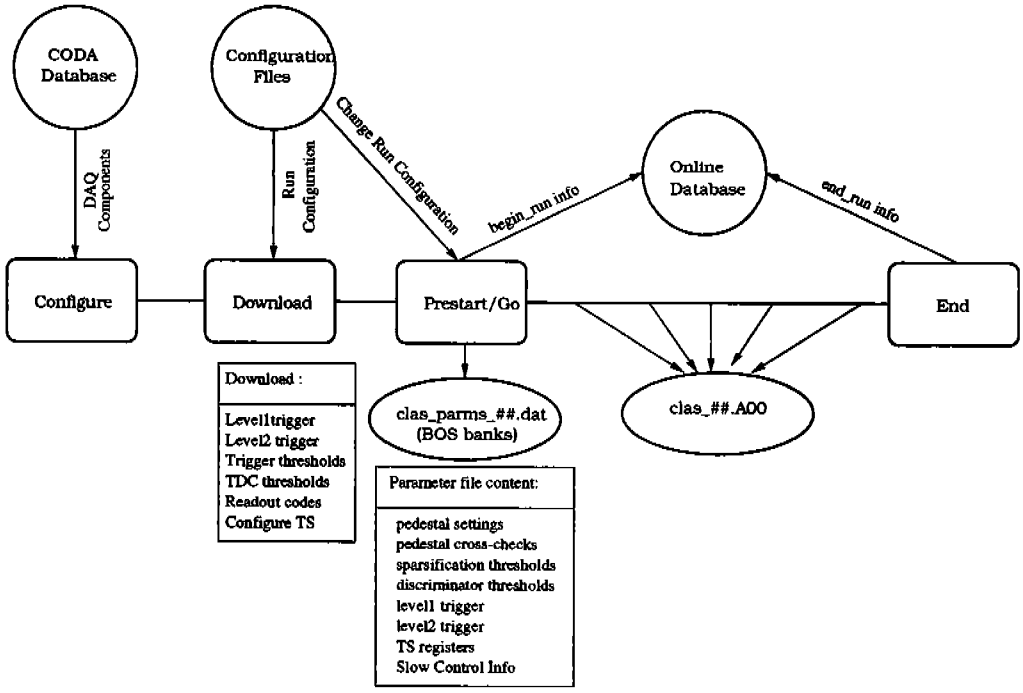

Fig. 19. Run control structure for CLAS.

A database provides the 'configuration' of DAQ components. This information coordinates the 'download' of all executable software into the VME readout controllers, and establishes corresponding processes, such as the Event Builder, on the SMPs and the workstations in the control room. In addition, during the download procedure all essential detector parameters, including the trigger supervisor (TS) configuration, the Level 1 and Level 2 trigger logic, and the trigger and TDC thresholds, are loaded from a run configuration file.

At 'prestart' the run parameters are read back from the hardware and compared to the original run configuration set. In case of a discrepancy a warning is issued. Essential run information about beam, target, and other run conditions is registered as 'begin run' information in an online database. The

prestart transition is concluded by reading back pedestals and sparsification thresholds and by writing all the run information, including some "slow control" information (magnet settings, target and collimator status, etc.), into parameters files.

At the 'go' transition the trigger is enabled, and data files are written in 2 GByte blocks. The data files contain physics events, as well as scaler readings and slow control information which are inserted into the data stream periodically. At the run 'end' transition, the final scaler readings are added to the data stream and the database.

3.9.3 DAQ Performance

The DAQ system can be viewed as a pipeline of processes that manipulate data and data transfer links between them, starting with the trigger and digital data conversion at the front-end and concluding with the data storage to RAID disks. The complete pipeline flows only as fast as its slowest component.

During CLAS commissioning, the event rate was limited to 400 Hz. The bottleneck in the data flow turned out to be the mechanism for transferring event fragments from the VME readout controllers to the Event Builder. The original scheme called for a "token" to be passed from readout controller to readout controller to collect corresponding event fragments into the event builder. This synchronous procedure was replaced with an asynchronous scheme where each of the 24 readout controllers pushes the event fragments in its output buffer over fast Ethernet lines into one of 24 "always open" input buffers of a multi-threaded Event Builder. This new procedure dramatically increased the accepted event rate from 0.4 kHz to about 2 kHz.

With that improvement, the event rate was limited by the interrupt, processing, readout, and network transfer times in the readout controller of approximately 300μs. This stage is represented by the open circles in Fig. 20. The live time was recorded while an electronic pulser varied the input rate, keeping the front-end conversion time fixed at 20 μs and the event size at 3 kByte. The livetime suddenly falls above 3 kHz because the readout and other activities in the front-end VME processors saturate the available CPU cycles. With the readout task moved to a RAM program of the Struck FASTBUS Interface (SFI) to decrease the readout latency, this sharp drop in the livetime is not seen until an event rate of 8 kHz (open squares in Fig. 20). The turn-over in livetime at this point is due to the data rate limit of 25 MByte/s for the local RAID disks at the back-end of the pipeline.

The pulser livetime measurements in Fig. 20 were obtained under controlled but somewhat artificial conditions. During actual data taking, the conversion time, event size, and trigger rate all vary depending on beam conditions.

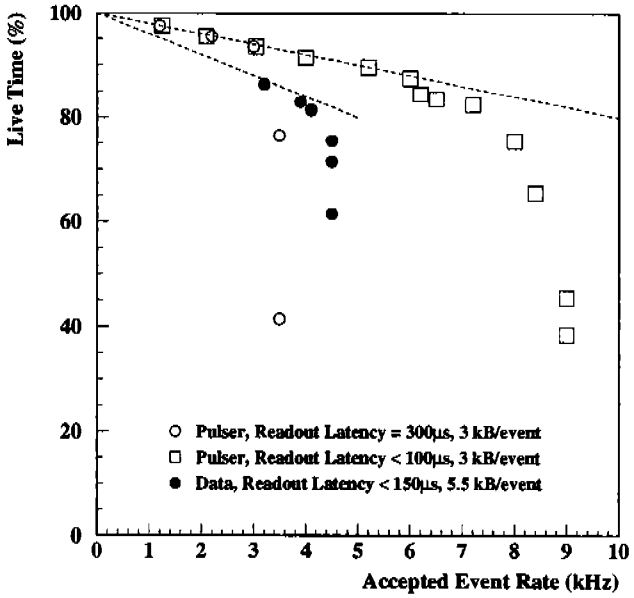

Fig. 20. DAQ performance expressed in terms of livetime vs. accepted event rate. Open symbols are data taken with an electronic pulser with the front-end conversion time fixed at 20 μs and an event size of 3 kByte. Test data simulating experimental conditions, shown as solid circles, were limited to 4.5 kHz by the data rate limit to disk of 25 MByte/s. The dashed lines show the effect on the livetime for front-end conversion times of 20 and 40 μs.

For example, for the 64-channel high resolution TDCs, the conversion time increases linearly with the number of input hits reaching 40 to 50 μs for a beam energy of 5.8 GeV and a current of 5 to 7 nA. This is also illustrated in Fig. 20 (full circles) for test data during an experimental run (EG2K). The trigger rate was varied by changing the trigger threshold at relatively constant beam current. At 4 kHz the livetime is reduced to 85%, which is consistent with a 40 μs front-end conversion time. For the experimental conditions in Fig. 20 the actual event size was 5.5 kByte, and thus we observe the sudden decrease in livetime at 4.5 kHz due to the 25 MByte/s data rate limit to disk.

4 Electron Beam Operations

This section describes the experimental apparatus used to characterize the electron beam properties. Table 1 lists the electron beam requirements for CLAS experiments. These reflect the CLAS detector capabilities, the experimental physics goals, the CEBAF beam, and diagnostic limitations at low beam currents (<10 nA). Luminosity limitations of the CLAS detector restrict the beam current range from 1 to 30 nA. A CLAS cryogenic target may have 15 μm-thick entrance and exit windows, and a diameter as small as 3.3 mm. The electron beam profile and halo requirements ensure that the

Table 1
CLAS electron beam properties.

Quantity	Range	Precision	Monitor
Energy	0.8 - 6.0 GeV	$\delta E/E < 0.1\%$	Beam Orbit Stability
Polarization	40-85%	$\delta P/P < 3\%$	Møller polarimeter
Position	± 3 mm of target center	100 μm	RF cavities
Width	$\sigma < 250$ μm	10 μm	Wire scans
Beam Halo	1:100000		Wire scans
Current	1-30 nA	$< 1\%$	Faraday cup

electron beam envelope fits within such a target window.

4.1 Electron Beam Position Monitors: Resonant Cavities

The electron beam position is measured continuously by three beam-position monitors (BPMs). Each of the three BPMs consists of three RF cavities. The three BPMs are located 36.0 m, 24.6 m, and 8.2 m upstream of the CLAS target. The third BPM is not used during photon beam experiments as it is downstream of the tagging bremsstrahlung magnet. These BPMs provide a beam position coordinate (x, y) and intensity measurement at each location. The low beam current results in a slow accumulation of charge and limits the measurement rate to about 1 Hz. The information from the BPMs is continuously used in feedback loops to keep the beam centered on the target. Every 20 seconds the position and current information is also inserted into the data stream.

The relative position calibration of the RF cavities is obtained via cross calibration with the beam profile monitors (see next section). Absolute position calibration is obtained by centering the electron beam in the upstream beamline quadrupoles, which have been surveyed into place. The current calibration is obtained via comparison with the calibrated Faraday cup. The RF cavities are very stable, so this calibration procedure is required once per week or less.

4.2 Electron Beam Profile Monitors: Harps

The electron beam profile is measured by moving thin wires (20 and 50-μm W and 100-μm Fe) through the beam and detecting the scattered electrons via Cerenkov light in the glass windows of photomultiplier tubes (PMT). The wires are oriented along the horizontal (x) and vertical (y) axes with the

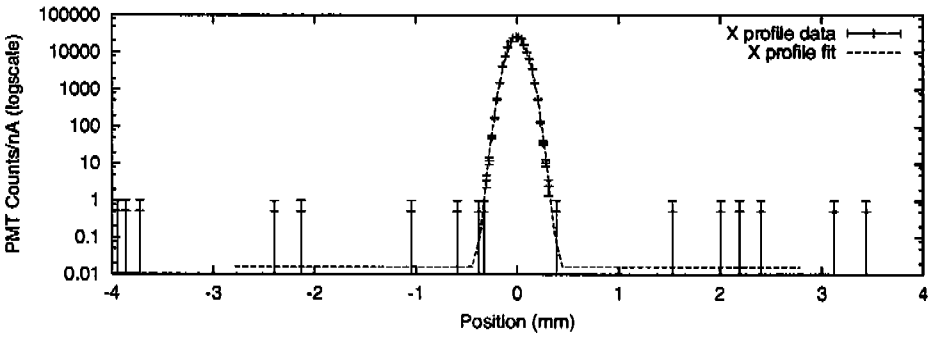

Fig. 21. Typical electron beam profile in the x-dimension measured by the harp located just upstream of the tagger magnet. The data are fit to a Gaussian with a constant background term. The sigma of the beam is 73 μm and the signal-to-halo ratio within $\pm 3\sigma$ of the centroid is 5×10^6.

direction of motion at 45° with respect to the horizontal axis. The wire-moving device is called a harp. There are three harps located at 36.7, 22.1, and 15.5 m upstream of the CLAS target. The PMTs are attached to the beam pipe, approximately 10 cm from the beam and are located 6.8 m upstream of the CLAS target. The harp motion is controlled by a stepper motor that is synchronized with a VME scaler readout of the PMT signals. Fig. 21 shows the results of a harp scan obtained online using a 5.8-GeV beam at 2-nA beam current. The beam profile is approximately round, resulting in a similar projection in the perpendicular (y-axis) view.

The harp scan procedure intercepts the beam and hence can only be performed when CLAS is not taking data. Harp scans are performed after any major change to the electron beam delivery or if other systems indicate problems with the electron beam.

4.3 Electron Beam Current: Faraday Cup

A Faraday cup composed of 4000 kg of lead, which corresponds to 75 radiation lengths, is located 29.0 m downstream of the CLAS target. The lead is supported on ceramic standoffs inside a vacuum chamber. An electrical feed-through provides a means to draw the deposited charge off of the Faraday cup. The electronics consist of a current-to-voltage converter followed by a voltage-to-frequency converter [32]. The typical operating gain results in one pulse corresponding to 0.11 pC of charge. The gain and offset of the system is checked via a calibration circuit that can be operated remotely whenever the electron beam is off.

In addition to measuring the integrated charge, the Faraday cup also measures the variation of the charge with helicity for experiments requiring polarized electrons [32]. The output of the voltage-to-frequency converter is sent to a

scaler with a FIFO and two latch bits. The latch bits record the helicity state of the beam, and the data are pushed into the FIFO at a rate of 30 Hz. The FIFO is analyzed to provide real-time information of the helicity-correlated charge asymmetry. This information is utilized at the source in a feedback loop to provide long-term (order of hours) minimization of any helicity-correlated charge asymmetry. The FIFO data are also included in the CLAS data stream.

4.4 Electron Beam Polarization: Møller Polarimeter

Beginning in Fall 1998, almost every running period has included polarized beam experiments, which now account for a significant portion of the Hall B physics program. A high-precision measurement of the beam polarization must be made in the hall to take full advantage of such a beam. A polarimeter that measures the asymmetry in elastic electron-electron (Møller) scattering has been installed in the hall for this purpose [33].

Similar to other polarimeters [34], the Hall B Møller polarimeter relies on detecting the scattered electrons in coincidence to determine the reaction kinematics. This method has the advantage, as compared to single-arm Møller polarimetry, of producing a clean data set without having to do energy-dependent background subtractions (see for example, Ref. [35]).

The Hall B polarimeter is located in the beamline immediately upstream of the bremsstrahlung tagging system (Fig. 2). The system consists of a target chamber, two quadrupole magnets, and two detectors in the horizontal plane on either side of the beamline. The target is a 25-μm-thick permendur foil that is magnetized with an approximately 100-G Helmholtz-coil system, producing saturated electron polarizations of about 8% along the plane of the foil. The foil is tilted at 20° with respect to the beamline. The two quadrupoles separate the scattered electrons from the unscattered beam. The two detectors are lead/scintillating fiber composites [36] located 7.0 m downstream of the target and 37.5 cm from the beam on either side of the beamline. The coincidence signal from the discriminated detector outputs is fed into a scaler that is read out for each helicity state of the beam. The layout of the system is provided in Fig. 22.

Measuring the beam polarization takes about 30 minutes and is typically done every other day. The statistical uncertainty from a Møller measurement is usually about 1% (absolute). The systematic uncertainty of the measured polarization is dominated by knowledge of the Møller target polarization (1.4% relative uncertainty). The other significant contribution to the systematic uncertainty is due to combined atomic-motion and finite-acceptance effects (0.8% relative).

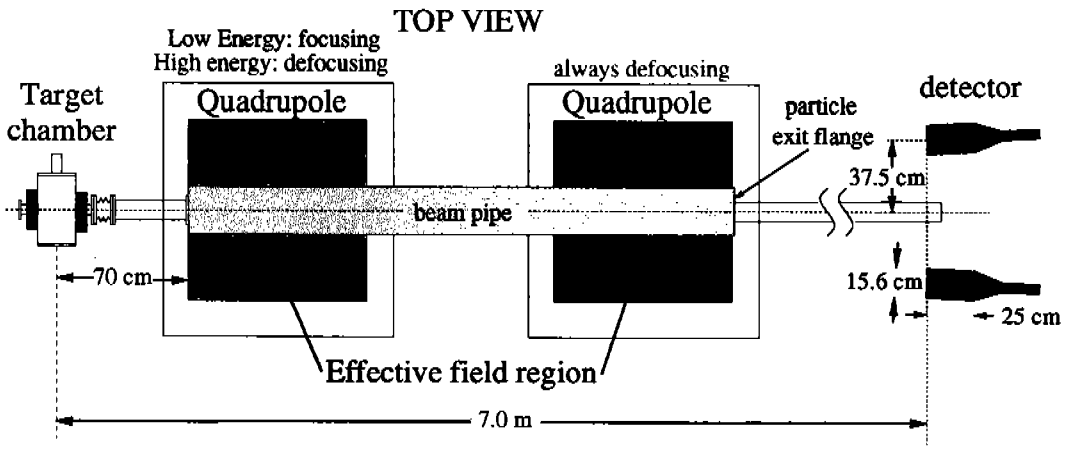

Fig. 22. Layout of the Hall B Møller polarimeter.

5 Photon Beam Operations

The photon-tagging system and its associated beamline components have been described in an earlier publication [37]. Electrons from the CEBAF accelerator strike a thin target (the "radiator") just upstream from a magnetic spectrometer (the "tagger"). Photons that are produced in the radiator continue toward the CLAS target following the same beamline through the magnet yoke that is traversed by the electron beam when the tagger is not in use.

There are three modes of operation for photon beams in Hall B: a normal non-polarized mode, a circularly polarized mode, and a linearly polarized mode. These are governed by the polarization state of the incident electron beam, and by the nature of the photon radiator, as described below.

5.1 Photon Production and Polarization

In the non-polarized and circularly polarized modes the photon beam is generated by passing the electron beam through a thin radiator, typically 5×10^{-5} to 3×10^{-4} radiation lengths of gold plated on a thin carbon support foil. The foil is located 0.5 m in front of the tagging magnet. Circular photon polarization results by polarization transfer when the incident electron beam itself is longitudinally polarized. Near the endpoint of the bremsstrahlung spectrum the polarization transfer is nearly 100% so the photons have the same level of polarization as the electron beam. For lower energy photons, the transfer is less efficient, so that when the photons have 50% of the incident beam energy the polarization transfer has fallen to about 60%. Determination of the photon circular polarization depends on the measurement of the degree of electron beam polarization and then very accurate theoretical calculations of the polarization transfer [38].

To obtain a linearly polarized photon beam, a thin diamond crystal, 20 to 50-μm thick, located 7 m before the tagging magnet, is oriented so that the channeling of the electrons through the crystal produces coherent, linearly polarized photons at certain energies. Rates of polarized photons on target of the order of 5×10^6 Hz are possible with this arrangement. In the linearly polarized photon mode the degree of linear polarization depends on the tight collimation of the photon beam, and reaches 80% in the coherent peaks with the parameters of our beam line. At the present time knowledge of the degree of polarization is determined from the known beam and target parameters using theoretical calculations.

5.2 Photon Beam Position and Profile

The electron beam used in photon experiments is monitored up to a point just before the radiator by the same instrumentation already described for electron beam operations. Thus, the production point and initial direction of the photon beam is well determined. Downstream of the tagging magnet the photon beam then passes through a collimator.

In the non-polarized case, the collimator has a 0.861 cm diameter hole in a cylindrical nickel block 25 cm long. This collimator is located approximately 14 m from the radiator, and restricts the diameter of the photon beam at the CLAS target to less than 3 cm. A magnet placed just downstream from the collimator sweeps aside low energy secondary charged particles created in the collimator.

With the linearly polarized photon beam, the nickel collimator is replaced by a combination nickel and tungsten collimator with a 2 mm diameter cylindrical hole, which restricts the size of the beam on the CLAS target to a diameter of less than 5 mm. This collimator is instrumented with detectors that assure the beam is correctly centered on the hole.

In all configurations, the photon beam position and size are monitored by a fixed array of crossed scintillator fibers located 20 m behind the CLAS target. The scintillators respond to the electron-positron pairs produced by photons in the CLAS target, in the atmosphere between the target and the hodoscope, or within the scintillating fibers themselves.

5.3 Photon Energy and Timing

The photon-tagging system can tag photons with energies between 20% and 95% of the incident electron energy E_0, and is capable of operating with elec-

tron beam energies up to 6.1 GeV. The field setting of the tagger magnet is matched to the incident beam energy so that those electrons that do not radiate will follow a circular arc just inside the edge of the pole face, and will be directed into a secondary shielded beam dump below the floor of Hall B with a maximum capacity of 800 W.

An electron that radiates a bremsstrahlung photon has lower momentum, and consequently smaller radius of curvature in the tagger dipole field, so that it emerges from the magnet along the open edge of the pole gap. A scintillator hodoscope along the flat focal plane downstream from this straight edge detects this electron, and thereby allows for the determination of the energy and timing of the radiated photon.

The overall geometry of this arrangement may be seen in Fig. 23. The tagger dipole is topologically a C-magnet with a full-energy radius of curvature of 11.80 m, a full-energy deflection angle of 30°, and a gap width of 5.7 cm. The required magnetic field in the gap is 1.13 T for a beam energy of 4 GeV.

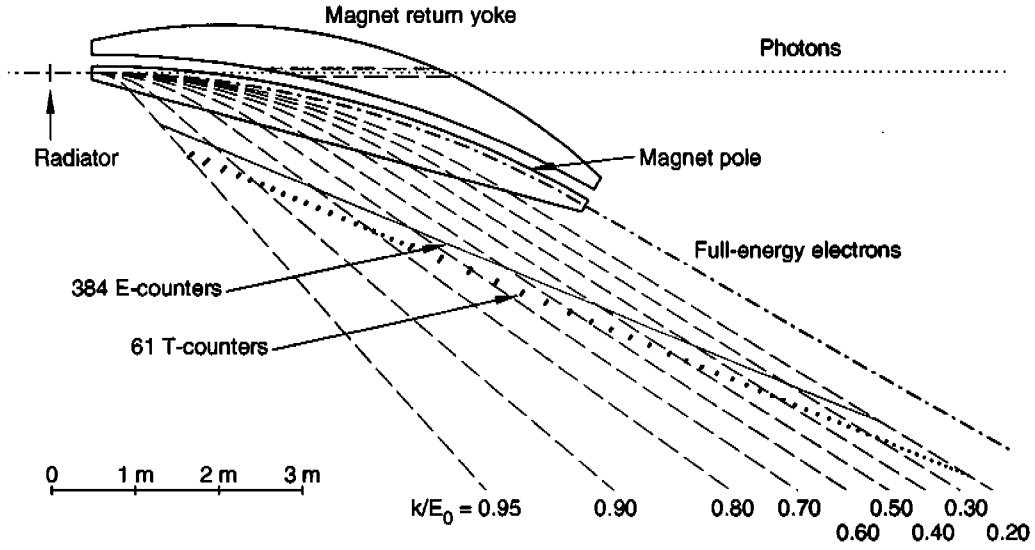

Fig. 23. Hall B photon-tagging system.

The focal-plane hodoscope consists of two separate planes of scintillator detectors. The first detector plane (called the E-plane for energy) is composed of 384 plastic scintillators 20-cm long and 4-mm thick. Their widths (along the dispersion direction) range from 6 to 18 mm in order to subtend approximately constant momentum intervals of $0.003 \times E_0$. Each counter optically overlaps its adjacent neighbors by one third of their respective widths, thus creating 767 separate photon energy bins that provide an energy resolution of $0.001 \times E_0$.

The second detector plane (called T-plane for timing) lies 20 cm downstream of the E-plane and contains 61 counters, 2-cm thick, which are read out using PMTs attached by solid light guides at both ends (transverse to the particle

direction) of each scintillator. The rms timing resolution of these counters is 110 ps.

5.4 Photon Beam Flux

The absolute photon flux is determined at very low flux rates by inserting a large lead-glass total absorption shower counter (TASC) into the photon beam. The TASC is essentially 100% efficient, which allows the tagging efficiency of the different elements of the tagging hodoscope to be determined. Due to counting pile-up problems, the TASC can only be operated at beam currents up to 100 pA, and must be retracted from the beamline under normal running conditions. Thus, secondary monitors, with absolute efficiency of only a few percent, but linear in flux over a wide range, are cross-calibrated against the TASC at low rates and then used to monitor the flux at higher intensities.

The first of these secondary monitors is a pair spectrometer, operated with a thin conversion foil in front of the spectrometer. In the early rounds of CLAS experiments the pair spectrometer was situated 22 m behind the CLAS target, near the TASC (see Fig. 2). This arrangement was not ideal since at high photon rates additional pairs produced in the CLAS target, and in the medium between the target and the pair spectrometer, caused pair rates that were too high and made the monitoring unstable. In addition, a sizable correction had to be applied to account for the photons lost in these pair production processes. More recently, a pair spectrometer has been installed in front of the CLAS target. By operating the entire system in vacuum, and by using a thin pair-conversion foil that removes less than 1% of the photons from the beam, it is possible to monitor the photon flux even at high flux rates.

A second method that uses out-of-time events allows the monitoring of any changes in the flux distribution of electrons associated with the production of tagged photons. Each time a photon-generated event is detected in CLAS, a TDC window, 200-ns long, is opened for each of the 64 timing detectors in the tagger hodoscope. Only the correct detector will record the correct time, but the other detectors will see random events, out of time with the true signal. This random rate is proportional to the total photon rate in the detector. Because of the high rate in the detectors, this has allowed the measurement of small rate changes (less than 1%) in time periods of less than 5 minutes.

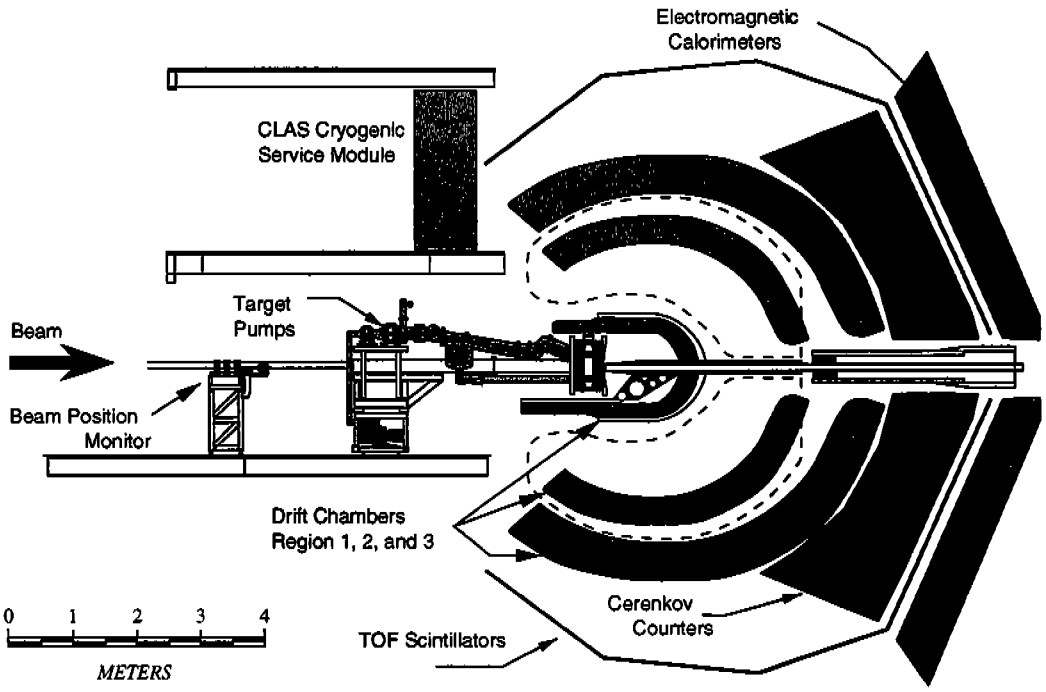

Fig. 24. A sketch depicting the positioning of the polarized target in relation to all major CLAS systems. The torus cryostats projected onto to the midplane are shown as dashed lines.

6 Operating Conditions

6.1 Targets

Hall B experiments are grouped into running periods according to beam type and target. A variety of targets have been used to date, with dimensions adapted to the particular needs of either electron or photon running. The most common target used has been liquid H_2. However, reactions have also been studied using liquid D_2, ^{3}He, and ^{4}He; solid ^{12}C, Al, Fe, Pb, and CH_2; and polarized NH_3 and ND_3 targets. All targets are positioned inside CLAS using support structures which are inserted from the upstream end, and are independent of the detector itself. A sketch of the insertion scheme for targets inside CLAS, together with the supporting equipment, is shown for the case of the polarized target for electron running in Fig. 24. Unpolarized targets have commonly been positioned inside CLAS at the center of curvature of the inner toroidal coil. A typical setup for electron running uses a 5-cm-long kapton cell (4-mm-diameter Al window) filled with liquid-hydrogen (or deuterium) in conjunction with a 7 nA beam current. The liquid-hydrogen targets used during photon-beam experiments are usually 10–18 cm long and wide enough to contain the bremsstrahlung photon beam which can be several centimeters wide.

Considerable data have been collected using polarized targets, and the special accommodations to the CLAS configuration deserves a brief description. Fig. 24 shows the polarized target [39] inserted into the field-free region of the CLAS detector. The various subsystems that comprise this target are a superconducting magnet, the 1 K refrigerator, the microwave and NMR systems, and the target module itself. The entire assembly, including the pumping system, is attached to a rail-mounted cart that can be rolled into and out of CLAS. The polarized target is positioned 0.57 m upstream of the center of the CLAS detector. This shift off center makes optimum use of CLAS components that would otherwise be shadowed by the target's field coils, and also contributes to background suppression as discussed below. With this target, the beam spot is rastered in a spiral fashion over a 1-2 cm diameter. The superconducting Helmholtz magnet produces a 5 T field parallel to the electron beam axis. At its center, the field is uniform to better than one part in 10^4 over a cylindrical volume of 20 mm in diameter and 20 mm long. This uniformity is necessary for dynamic nuclear polarization. The on-axis bore of the magnet is 200 mm in diameter, and provides a $\pm 55°$ open aperture for particles scattered into the forward cone.

6.2 Luminosity Constraints on CLAS Operation

CLAS is designed to operate efficiently at a luminosity up to 10^{34} nucleon $cm^{-2}s^{-1}$. However, in some situations the actual operating luminosity is restricted due to other factors. For example, at very low values of Q^2 the experiments are limited by the DAQ rate. For tagged-photon beam experiments, the photon flux is often chosen to limit the accidental rate between the tagging system and CLAS in either the trigger and/or the final data analysis. Note that accidental coincidences within CLAS are very low due to the low particle fluxes involved. In this section we concentrate on the luminosity limitations imposed by the detector itself.

The detector components are most severely challenged during electron scattering experiments at high Q^2, when the maximum tolerable luminosity in CLAS is generally limited by the large flux of Møller electrons and associated X-rays produced from the target by the multi-GeV incident electron beam. This constraint is most severe for the drift chambers, particularly R1, since they are very sensitive to low-energy X-rays. A large number of background-related hits in the chambers makes track reconstruction difficult. Also, the effects of sustained high luminosities are unfavorable for long chamber lifetimes. See Ref. [8] for more details, including lifetime estimates.

The operation of a detector completely unshielded from electromagnetic background would be limited to luminosities well below 10^{34} $cm^{-2}s^{-1}$. Therefore,

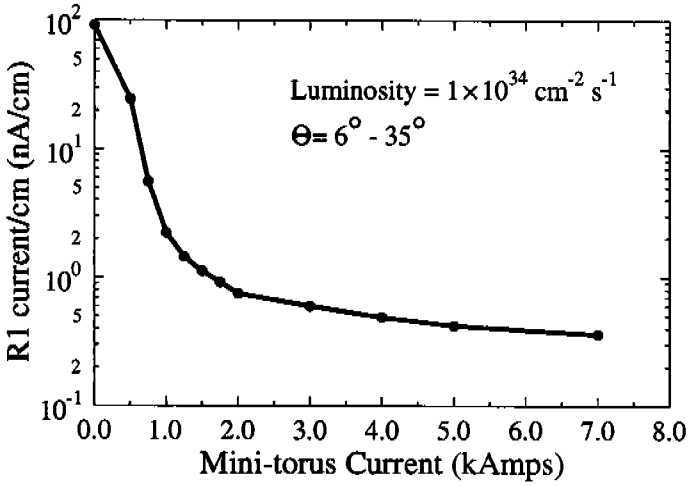

Fig. 25. Measurement of R1 sense-wire current per cm of wire length as a function of the mini-torus current.

as previously mentioned, an inner, normal-conducting, toroidal magnet is radially positioned between all unpolarized targets and the R1 drift chamber assembly during electron-beam operations. This "mini-torus" is designed to focus Møller electrons onto a lead absorber surrounding the beam pipe immediately downstream of the target. (With the polarized target, the large size of the Helmholtz assembly prohibits use of the mini-torus, but the upstream placement of that target allows its own field to play a similar role in keeping such electrons away from the R1 chambers.)

Fig. 25 shows the average currents drawn by the R1 drift cells at forward angles as a function of the current in the mini-torus. By confining the expansion of the flux of Møller electrons, this magnet reduces the chamber currents by more than two orders of magnitude at its nominal operating current of 6000 A.

The tracking efficiency decreases at high luminosity by approximately 1% per 1% increase in chamber occupancy (see Ref. [8] and Section 3.2). As shown in Fig. 26, the efficiency is significantly degraded beyond a R1 occupancy of 4%, so we set an operational limit of 3% occupancy in R1 for normal electron runs. The occupancy during photon-beam experiments is smaller by more than an order of magnitude.

For low-Z targets, the luminosity limitation is due to the production of Møller electrons and, therefore, inversely proportional to the atomic number Z. Fig. 27 shows the operating luminosity for various targets, which increases linearly as a function of Z for most targets. For the liquid-hydrogen target (Z=A), the luminosity is limited to 0.9×10^{34} $cm^{-2}s^{-1}$. However, the scaling as a function of Z breaks down for high-Z targets (e.g. Fe) because of the increased production of X-rays in the target.

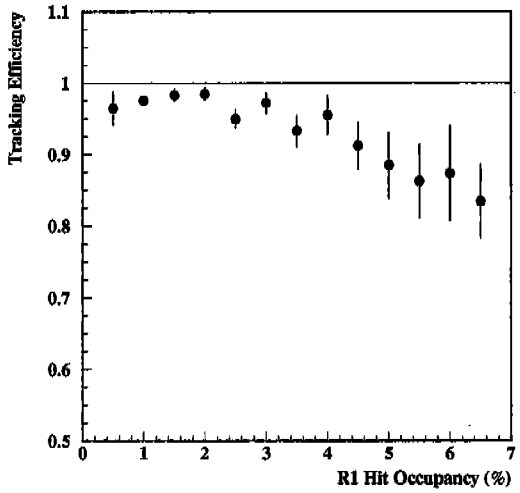

Fig. 26. Tracking efficiency as a function of drift chamber occupancy. The efficiency begins to fall off for occupancies in R1 greater than 3%.

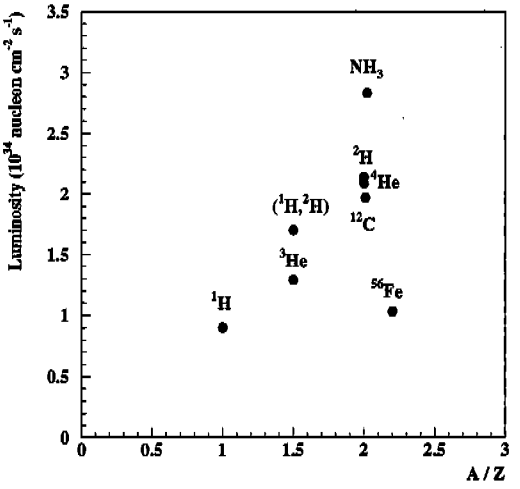

Fig. 27. Maximum luminosity as a function of A/Z for a constant occupancy of 3% in R1. Experiments operating at slightly lower occupancy were scaled up to ease comparison. The polarized NH_3 target was shielded by the polarizing solenoidal field and could run at higher luminosity. A dual hydrogen and deuterium target cell is indicated by (^{1}H,^{2}H).

6.3 Operating and Maintenance Experience

CLAS was commissioned during 1997 and has been in routine data taking mode since then. The superconducting magnet, the detector components, and the electronics and data acquisition systems have worked reliably; the average availability of the detector exceeds 85%. The most critical components are the data acquisition system and the drift chambers. Both are complex systems in which high channel count increases the likelihood of component failure. Most DAQ problems can be fixed within minutes or hours, sometimes from off-site.

In the drift chambers, broken wires may cause high-voltage shorts and paralyze an entire drift chamber section. Since there is enough redundancy in the tracking system, this can be handled by making an access to the hall and removing high voltage from the affected area. Broken wires are then removed during the next available regular maintenance period. Access to the R2 and R3 drift chamber pre-amplifiers and to the wires requires moving the forward carriage and the two sideways carriages away from the central detector. Fixtures are then installed that allow the Region 3 chambers to move out radially by about 1 m. This procedure is labor-intensive; the repair of a single Region 3 chamber takes a minimum of four weeks. Since 1997, a total of 55 sense wires have been removed. Broken wires are likely due to unplanned temperature excursions in the hall, and the rate has slowed since we have implemented careful controls over the environment.

7 Event Reconstruction

Event reconstruction in CLAS consists of the identification of charged and neutral particles along with the computation of their 3-momenta. Charged-particle reconstruction requires both particle tracking and particle time of flight. The tracking information is used to determine the particle momentum (p) and flight path, while the time of flight gives particle velocity (β) when combined with flight-path information. The momentum and velocity information are combined in the usual way to give the particle mass: $m = p/\beta\gamma$. Electron identification additionally requires the track to match in time and position with both a CC hit and an isolated energy cluster in the EC. The track momentum must also be consistent with the EC energy deposition.

Neutral particles are detected in either the calorimeters or SC (or both). The reconstruction begins by finding isolated clusters of energy, and determining the spatial location, deposited energy, and the time of the cluster. Neutral particle candidates are identified as clusters in the outer detectors that do not match any charged-particle track. For photons that deposit all of their energy in the calorimeters, the energy is calculated from the signal pulse-height in the calorimeters. The momenta for neutrons are calculated from their flight time as determined by the time signal in the calorimeters and, when relevant, the matched TOF counter. In either case, the angle of the neutral particle trajectory is determined from the position of the cluster at the face of the calorimeters.

For all events, precise determination of the interaction time or event start time is required. For electron running, the event start time is derived from the arrival time of the electron at the TOF counters, corrected for flight path and signal delays. As shown in Fig. 28, the average time resolution for recon-

structed electrons in CLAS is 150 ps. For photon-beam running, the tagged electron (recorded in the tagger T counters) determines the arrival time of the radiated photon at the target. The resolution of the tagging spectrometer is 110 ps. A more accurate event start time is obtained by replacing the measured electron start time (or the tagger time) by the 499 MHz accelerator RF signal that determines the beam bunch associated with the event. In this way, the event start time can be determined to within the few ps width of the beam bunch.

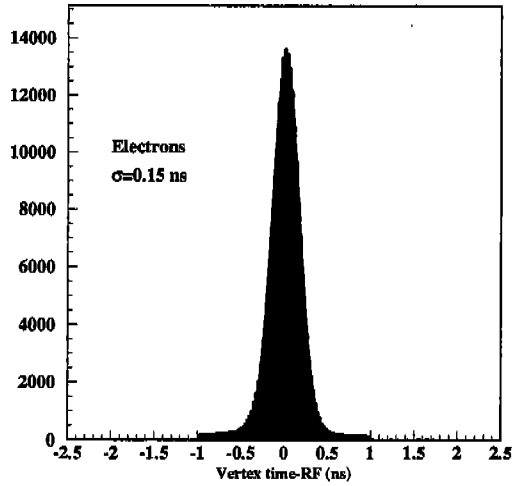

Fig. 28. Reconstructed vertex times for electrons compared to the accelerator RF signal, summed over all kinematics. Electron times are clipped to ± 1 ns, the time between RF buckets.

7.1 Charged Particle Tracking

Tracking in the inhomogeneous magnetic field [40] proceeds in four steps. The first three steps are necessary before proceeding with hit-based (HBT) track fitting, followed by time-based (TBT) track fitting.

(1) cluster finding: The first step is to find a contiguous group of hits (called a cluster) in each of the superlayers. Each cluster may contain several track segments.
(2) track segment finding: A lookup table is used to find groups of hits or segments within one cluster that are consistent with a track traversing a superlayer.
(3) segment linking: Segments from individual superlayers are identified with segments in other superlayers, again using a look-up table. If the look-up table address corresponds to a possible track, it also contains an estimate of the track's initial parameters.
(4) track fitting: Using the linked segments, a preliminary angle and momentum are assigned and a trial track is propagated through the CLAS

magnetic field. At each layer we calculate the distance-of-closest-approach (DOCA) of the track to the hit wire (HBT), or to the position derived from the drift times (TBT). As described below, track parameters are then adjusted to provide the best fit of the track to the measured positions.

The trajectory of each charged particle is determined by a set of five parameters $\vec{q}$ corresponding to the inverse momentum, the polar and azimuthal angles (with respect to the beam), and the interaction vertex transverse to and parallel to the beam direction. The vector $\vec{q}$ is determined by fitting positions from a reference trajectory ($d_i(\vec{q})$) to the wire positions during HBT and to the measured DOCA during TBT [40]. The fitting procedure minimizes the quadratic form:

$$\chi^2 = \sum_i \frac{[d_{meas,i} - d_i(\vec{q})]^2}{\sigma_i^2}, \tag{4}$$

where the uncertainty for HBT is given by $\sigma_i \sim$ cell size / $2\sqrt{12}$, and for TBT by a distance-dependent resolution which varies between 200 and 800 μ (see Fig. 8). The procedure converges after a few iterations.

Because the drift time only predicts the distance of the track from the wire and not which side of the wire the track was on, it is necessary to resolve the left-right ambiguity in each wire layer before the track is propagated through the CLAS and before the final track fit. This ambiguity is resolved locally within the superlayer. A straight-line fit is made to various hit choices within one superlayer cluster, trying all possible left-right combinations, and selecting the one with the highest probability. This selection is then used by the global track propagation and the final fitting routines. If, in resolving the local left-right ambiguity, the wrong combination is chosen, the entire track can be lost due to a failure of the global χ^2 cut. To reduce this inefficiency, the global track angle from the HBT fit at the superlayer is required to agree with the local angle found from fits to the individual segments.

7.2 Monte Carlo Simulation

The CLAS Monte Carlo simulation program, GSIM, implements a complete model of the detector using the GEANT 3.21 [41] libraries from CERN. These libraries model the propagation of particles through different materials including all physics processes, such as multiple scattering, energy loss, pair production, and nuclear interactions. The simulation program is built using these GEANT routines to define a large number of geometrical volumes of different materials, and then tracing particles through these volumes. Charged particles

will also be subjected to the effects of the magnetic field, which uses the same field map as is used by the track reconstruction programs. All the active detection volumes of CLAS are accurately modeled from engineering drawings and actual measurements of the detector. In addition, most of the passive support structures are also included to a high degree of accuracy. Special subroutines for each active part of the detector model the detector response in detail, so that the resulting output of the GSIM simulation accurately resembles the output of the real detector.

A typical simulation run starts with an *event generator* that produces an input file of four-vectors of the particles to be traced through the detector. This file is then fed to the main simulation program, GSIM, which produces a simulated data file. This simulated data file represents the data that one would obtain with a perfectly working detector. To include the effects of less-than-perfect detector response, due to broken drift wires, problematic phototubes, etc., the output of GSIM is passed through a separate post-processing program. This final output can then be analyzed using the same tools as are used to analyze real data. Throughout the remaining discussions, CLAS data are compared to the results of these Monte Carlo simulations.

8 Detector Performance

8.1 Acceptance

The superconducting coils of the CLAS torus are housed in six-inch-thick cryostats that divide the full solid angle into the six sectors. At forward scattering angles, the cryostats come together, reducing the azimuthal phase space to zero. The coils occlude about 15% of the azimuth at 90° and about 50% at the forward angle of 15°. The acceptance for particles of finite momentum depends on whether the particles are bent toward or away from the beamline. Fig. 29 shows the electron yields at a beam energy of 1.6 GeV as a function of the angles θ and ϕ at the target. At this kinematics, the highest momentum electrons fail to reach the forward detectors for scattering angles less than approximately 20°.

Single-particle acceptances are particularly relevant to photoproduction experiments, where many exclusive channels can be measured by detecting a single particle in CLAS in coincidence with a hit in the tagging spectrometer. For example, the acceptance of exclusive π^0, π^+, and η production in photoproduction reactions like $\gamma p \to p\pi^0$ or $\gamma p \to \pi^+ n$ is given by the reconstruction of a single charged track in CLAS. For electroproduction, the same channels require in addition the detection of the scattered electron.

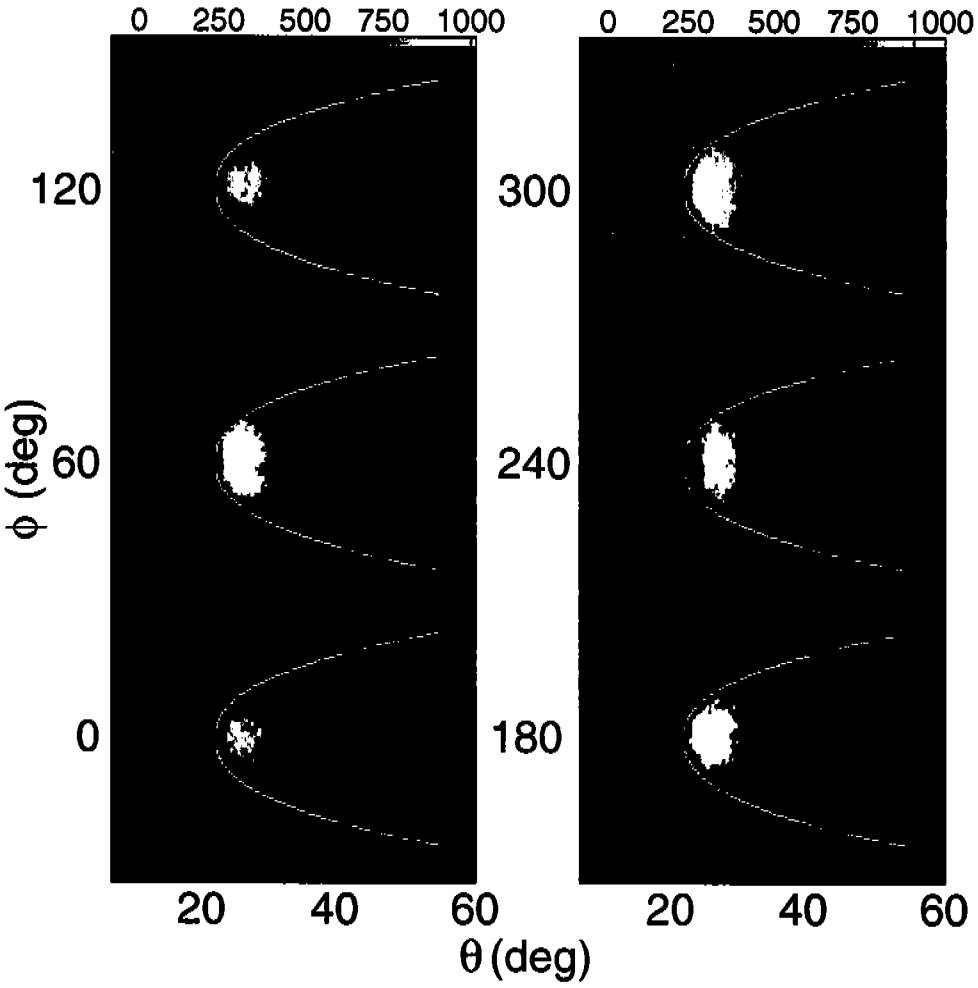

Fig. 29. Yield of scattered electrons in CLAS in ep reactions with a beam energy of 1.6 GeV showing the coverage in azimuthal angle ϕ_e vs. scattering angle θ_e for inbending electrons. The acceptances of the six sectors are separated by the six coils of the toroid. The lines indicate the fiducial volume cuts, eliminating a band of particles at low angles that produce direct light into the Cerenkov counter PMTs without using the mirror system.

In order to decrease systematic uncertainties due to acceptance uncertainties, a fiducial volume is defined inside of which the acceptance is large and uniform. The definition of the fiducial volume varies from experiment to experiment, but we discuss typical examples for illustration. We consider non-decaying neutral or charged particles that emanate from the target region. For each particle type, neutral, positively and negatively charged, the surface of the fiducial volume is a unique function of the momentum, scattering angle θ, and azimuthal angle ϕ of the particle. Fig. 29 shows typical fiducial cuts as a closed contour in θ and ϕ for electrons with data overplotted.

CLAS is often used to detect two outgoing particles with one undetected particle in exclusive meson production reactions. The coverage in center-of-

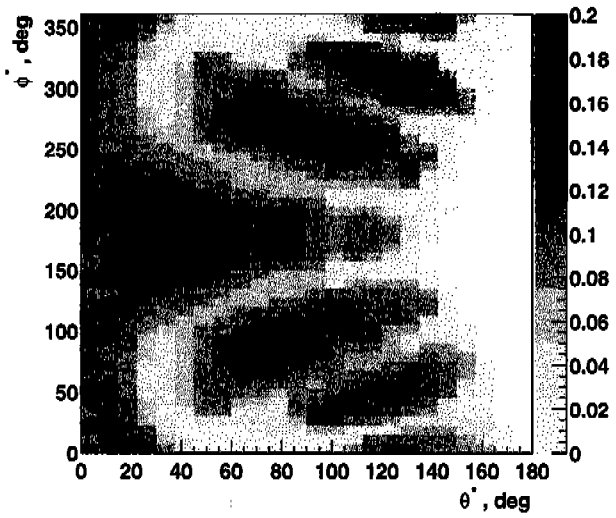

Fig. 30. Contour plot of the acceptance for detecting the scattered electron and the produced π^+ meson of the reaction $ep \rightarrow e'\pi^+(n)$ as a function of the the pion center-of-mass angles (θ^* and ϕ^*) in a bin of Q^2 between 0.5 to 1.0 (GeV/c)^2 and W between 1.1 and 1.3 GeV.

mass coordinates for the meson is an important ingredient in the analysis. In Fig. 30 is shown the acceptance for $ep \rightarrow e'\pi^+(n)$ in the center-of-mass coordinate system. This figure is for a fixed bin in Q^2 and hadronic mass, W. The depleted areas correspond to the uninstrumented regions occupied by the six toroid coils transformed to the center-of-mass frame. The coils join together at the beamline in the forward direction, indicated by the depletion of events for ϕ^* at 0 and 360° ($\theta^* \sim 60°$). The absence of events at large angles in the center-of-mass ($\theta^* \gtrsim 150°$) is due to the maximum coverage of the drift chambers to 140° in the laboratory frame, as well as the cutoff of low momentum particles at very large angles.

8.2 Charged Particle Detection

After imposing fiducial requirements to cut out areas of low acceptance, the CLAS performance can be characterized by its efficiency to detect charged and neutral particles that enter the defined fiducial volume. The chambers have layer efficiencies exceeding 98% (Section 3.2). In addition, noise hits and dead areas due to equipment malfunctions affect the tracking efficiency. To mitigate the effect of take dead areas, the tracking algorithm requires the presence of a track segment in only five of the six superlayers.

As an example, the efficiency for detecting pions was determined via the overdetermined $\gamma p \rightarrow p\pi^+\pi^-$ reaction. Each time a p and π^- pair is found, the missing mass is calculated and the three-momentum is computed for candidates within tight limits for the π^+ missing mass. If the predicted momentum vector falls within the fiducial cuts, the tracking output is searched for a pos-

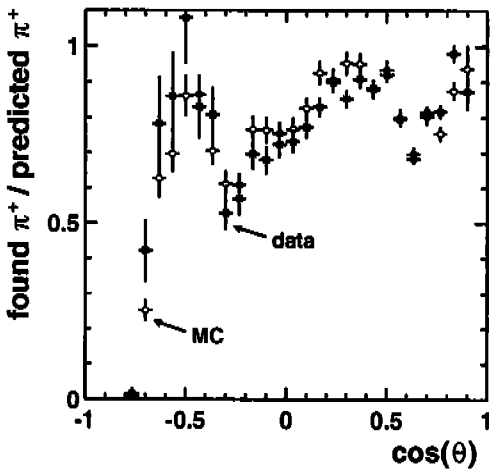

Fig. 31. Ratio of π^+ particles found compared to those expected within the detector fiducial volume using the reaction $\gamma p \to p\pi^+\pi^-$. The ratio is plotted both for data and Monte Carlo. The selected momentum range of π^+ is between 0.24 and 0.27 GeV/c. The agreement shows that inactive areas of the detector are well modeled by the simulation.

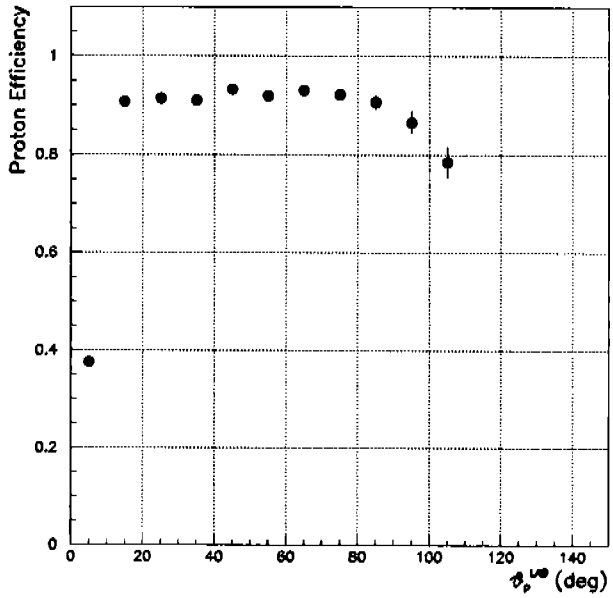

Fig. 32. The efficiency for detecting protons in sector 6 as determined from the over-constrained reaction $\gamma D \to pp\pi^-$. The selected protons were in a momentum range between 0.4 and 2.1 GeV/c.

itively charged track. The ratio between found and predicted tracks is plotted for data and Monte Carlo in Fig. 31 as a function of $\cos\theta$ for momenta between 0.24 and 0.27 GeV/c. A ratio less than one indicates that some detector elements were inactive during this data taking period. The curves to not go to zero, since they are averages over all CLAS sectors. The selected momentum range is rather low for CLAS, but chosen to cover a very broad range of angles

with a single reaction. The inefficiencies in the detector at the time of data collection are especially pronounced in the backward region of CLAS, but are nevertheless well reproduced by the Monte Carlo simulation, showing that the detector response is modeled correctly. In a second example, Fig. 32, we show the efficiency for detecting protons in a single sector which was determined from the data using the over-constrained reaction $\gamma D \rightarrow pp\pi^-$. The efficiency determined in this manner is higher than 90%, and uniform from sector to sector, over most of the available kinematic range.

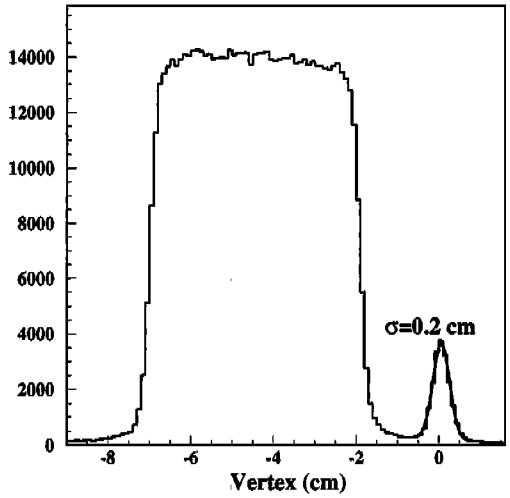

Fig. 33. The reconstructed interaction point along the beam for electron tracks traced back to the target. The data set is for a beam energy of 5.7 GeV. The thin foil at the origin provides a measure of the z-vertex resolution, $\sigma = 0.2$ cm.

The interaction vertex of charged particles can be reconstructed by tracing the reconstructed trajectory of particles in the drift chambers back to the target. The precision of the tracking is illustrated in Fig. 33 using the apparent width of a foil in the beam immediately downstream of the 5-cm hydrogen target using identified electrons. The 2-mm width is determined entirely by the resolution of the tracking system back to the vertex position along the beam direction, but depends on the electron angle, which ranges from 20 to 40°.

After the initial event reconstruction is completed, some invariant quantities, such as reconstructed masses, still depend weakly on kinematical variables. This effect is illustrated in Fig. 34a, where the reconstructed mass of the undetected neutron is plotted for the reaction $ep \rightarrow e'\pi^+(n)$ as a function of the laboratory azimuthal angle ϕ of the electron. This false dependence is likely due to a combination of imperfect placement of the coils inside the magnet cryostats and misalignments of the drift chamber system. Empirical corrections applied to the magnitude of the reconstructed momentum as a function of θ and ϕ eliminate the observed unphysical dependence on kinematical variables. The corrections are determined for kinematics that match those of a particular experiment to improve their applicability. For the example given,

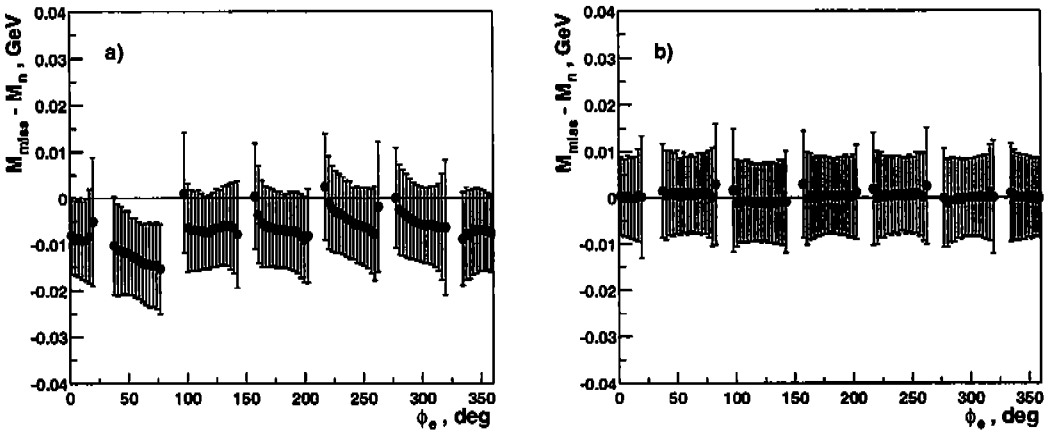

Fig. 34. The peak position and width (indicated by the error bars) of missing mass in the reaction $ep \rightarrow e'\pi^+(n)$ relative to the neutron mass is plotted as a function of the azimuthal angle ϕ. The plots are produced a) before and b) after empirical corrections to the electron momentum. The groupings correspond to the six sectors.

the corrections were obtained from elastic scattering and applied to π^+ production at 1.515 GeV. After the magnitude of the momentum was corrected, the missing mass was reconstructed as shown in Fig. 34b. The momentum corrections are most important at forward angles and of the order half a percent or less, i.e., comparable to the momentum resolution. Details of the corrections for various analyzes can be found in Refs. [42–44]. These corrections have been applied to all subsequent data.

Elastic electron-proton scattering events are used to study the CLAS momentum and angular resolution. The electron angle is used to predict the proton momentum, which is then compared to the measured value. The sigma of the differences between the predicted and measured values are shown in Fig. 35. Also shown are the same quantities determined from the GSIM simulation. The drift chamber intrinsic resolution function was determined from a study of residual distributions from charged tracks and parameterized as a Gaussian with width varying as a function of the distance-of-closest-approach (DOCA) of a track to a wire (Fig. 8). However, it was necessary to scale up the size of this smearing function by a factor of 1.7 in order to match the momentum resolution of the data shown in Fig. 35. The difference between the single-superlayer resolution and the actual resolution is due to uncertainties in the absolute position of one chamber relative to the others in the tracking system. The scaled resolution function in the Monte Carlo program was used to predict the single-particle momentum and angular resolution. It is worth commenting on the resolution increasing as a function of momentum. Because these plots were obtained using elastic scattering events, the higher momentum particles are scattered at small angles where the toroid has higher magnetic field. The momentum resolution at a fixed angle, illustrated below, shows a different behavior.

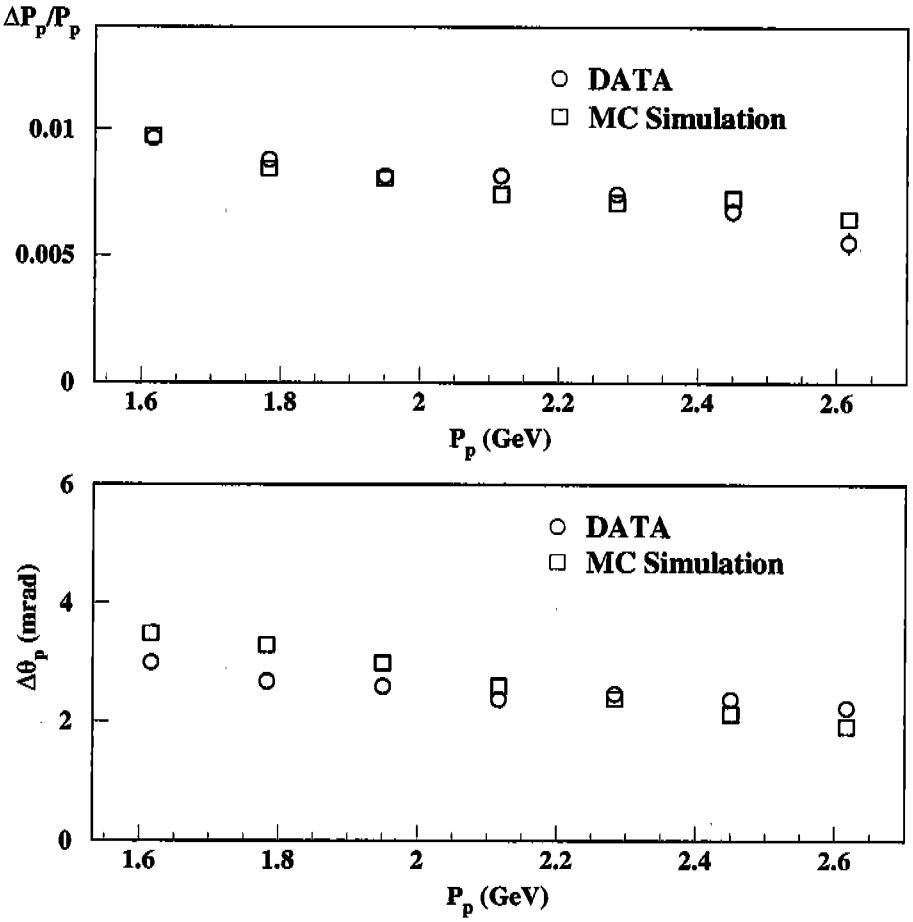

Fig. 35. Momentum and angular resolution for protons as determined from the measured angle of the scattered electron. The procedure is repeated for Monte Carlo generated elastic scattering events for direct comparison with the data. To match the measured resolution, the single-superlayer position uncertainties were increased by a factor of 1.7. The error bars are within the size of the data symbols.

The momentum resolution of CLAS changes significantly as a function of angle due to the strong variation of magnetic field between small and large angles, making a simple description of the resolution impossible. For the purpose of illustration, a parameterization of the momentum and angular resolution at a fixed scattering angle (35°) is given to indicate the dependencies on kinematical quantities. In Figs. 36 and 37 the simulated fractional momentum resolution for electrons and protons at a scattering angle of 35° is given for two values of the toroid current as a function of particle momentum. There is very little variation between particle type and charge, as expected. The dependence of the resolution of the scattering angle and azimuthal angle on momentum is shown in Figs. 38 and 39. The momentum and angular resolutions at 35° can be parameterized as:

$$\frac{\sigma_p}{p} = \frac{I_o}{I}\sqrt{\sigma_1^2 p^2 + \left(\frac{\sigma_2}{\beta}\right)^2},$$
$$I_o = 3375\,A,\ \sigma_1 = 0.33\,\%\,GeV^{-1},\ \sigma_2 = 0.18\,\% \tag{5}$$

$$\sigma_\theta = \sqrt{\sigma_1^2 + \left(\frac{\sigma_2}{p\beta}\right)^2},\ \sigma_1 = 0.55\,\text{mrad},\ \sigma_2 = 1.39\,\text{GeV}\cdot\text{mrad} \tag{6}$$

$$\sigma_\phi = \sqrt{\sigma_1^2 + \left(\frac{\sigma_2}{p\beta}\right)^2},\ \sigma_1 = 3.73\,\text{mrad},\ \sigma_2 = 3.14\,\text{GeV}\cdot\text{mrad}. \tag{7}$$

Roughly speaking, the fractional momentum resolution varies between one half and one percent. The polar angle resolution is approximately 1 mrad, while the resolution on the azimuthal angle is approximately 4 mrad. Note that the fractional momentum resolution increases with momentum, while the angular resolution decreases; these trends are consistent with contributions coming from measurement errors (σ_1) and from multiple scattering (σ_2). For both the momentum and θ resolution, the two terms are comparable over the momentum range of interest; the position measurements with stereo wires dominate the ϕ resolution.

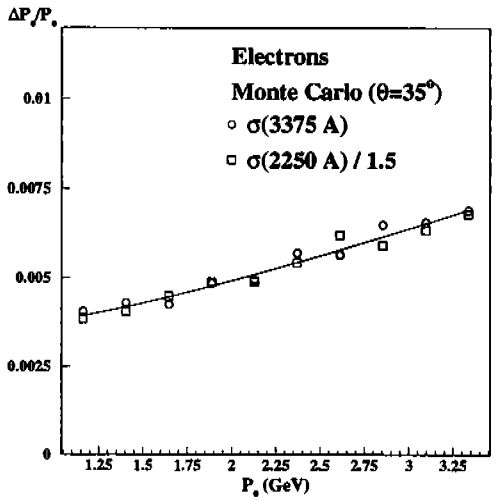

Fig. 36. Fractional momentum resolution for electrons at a scattering angle of 35° as determined by Monte Carlo at two different magnetic field settings. The momentum resolution scales with the inverse of the field.

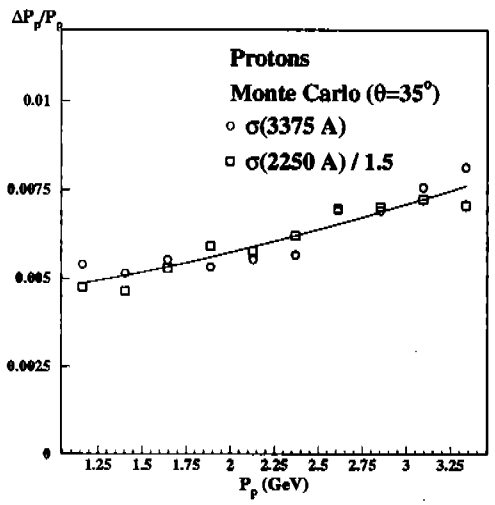

Fig. 37. Fractional momentum resolution for protons at a scattering angle of 35° as determined by Monte Carlo at two different magnetic field settings. The momentum resolution scales with the inverse of the field.

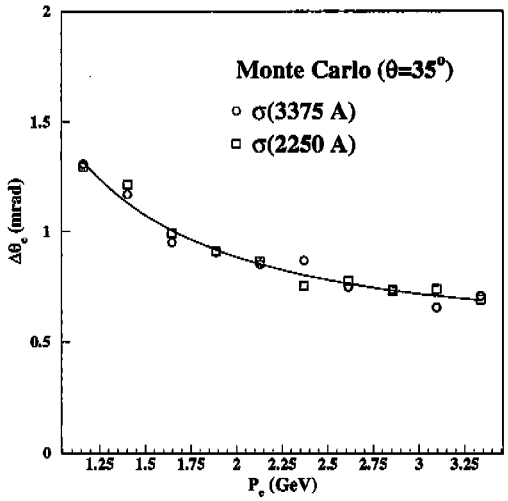

Fig. 38. Resolution in the scattering angle for electrons at 35° as determined by Monte Carlo at two different magnetic field settings. The angular resolution is independent of the field setting.

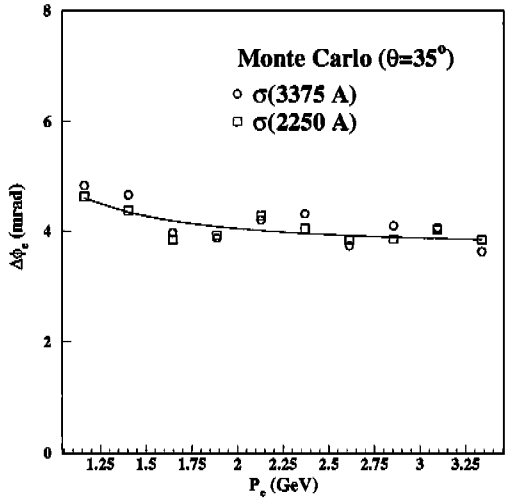

Fig. 39. Resolution in the azimuthal angle for electrons at a scattering angle of 35° as determined by Monte Carlo at two different magnetic field settings. The angular resolution is independent of the field setting.

8.3 Neutral Particle Detection

Single neutral particles (photons or neutrons) are defined as an isolated cluster of energy deposition in the calorimeters that is not consistent with any charged track. Monte Carlo simulations predict a 50% detection efficiency for 100 MeV photons, 95% for 200 MeV, and greater than 99% for energies greater than 250 MeV. The neutron detection efficiency of the forward calorimeter has been determined by tagging neutrons via the $ep \rightarrow e'\pi^+ n$ reaction. The measured efficiency rises linearly from 5% at 0.6 GeV/c to 45% at 1.8 GeV/c, and levels off at a plateau value of 50% above 2 GeV/c. Fig. 40 displays the neutron detection efficiency versus momentum [45,46].

The reconstructed mass of π^0 mesons via two photons is used to demonstrate the precision with which photons can be reconstructed in the calorimeter. Neutral hits in the calorimeter are identified by the absence of a matched track in the drift chambers. The invariant mass of events with two neutral hits in any of the forward-angle calorimeters is shown in Fig. 41, demonstrating clear peaks at the π^0 and η masses for a beam energy of 5.7 GeV. The measured π^0 mass width for photons detected within a single module of the EC and restricting the opening angle between photons to be less than 25° is about 18 MeV/c^2 [13].

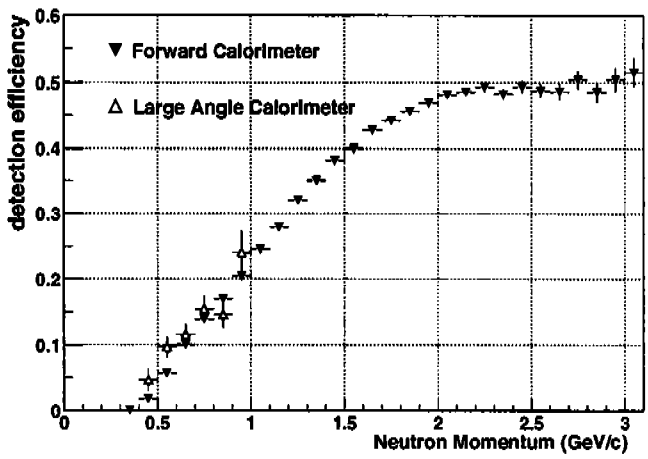

Fig. 40. Neutron detection efficiency in the EC and LAC as a function of the neutron momentum. The error bars are binomial in both cases. The measured momentum range in the LAC is smaller than in the EC due to the angular distribution of neutrons in the calibration reaction used ($e + p \rightarrow e + \pi^+ + n$), which is peaked in the forward region.

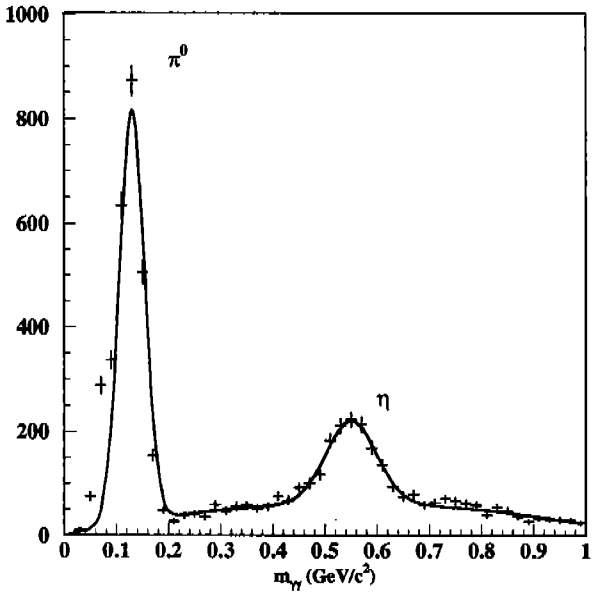

Fig. 41. Reconstructed invariant mass of two-photon events in the EC, featuring reconstructed π^0 and η mass peaks. The data are taken from an electron run with a beam energy of 5.7 GeV.

8.4 Particle Identification

Electrons are selected using the EC and CC detectors and, for exclusive reactions where kinematics constrain the reaction, the misidentification probability is negligible. However, for inclusive or semi-inclusive reactions, the cleanliness

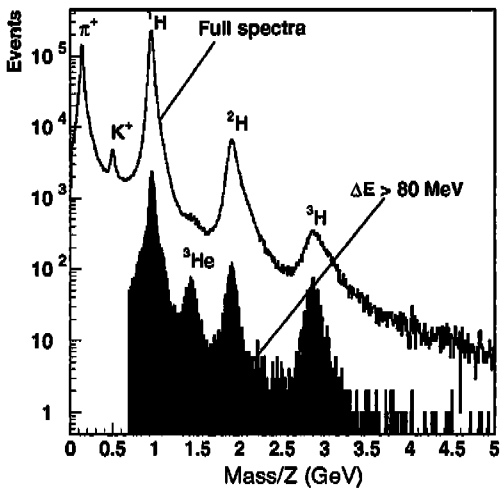

Fig. 42. Reconstructed mass/Z for positive tracks from a carbon target. Additional sensitivity to high-mass particles is obtained by requiring large energy loss in the scintillators (shaded histogram).

of the electron sample must be understood. The CC threshold for pions is 2.5 GeV/c (Section 3.3), but nevertheless pions may be counted due to the production of δ-electrons in the material preceding or within the counter. GSIM estimates that the efficiency for detecting pions below 1 GeV/c is $\lesssim$1%. Therefore, based on the CC alone, π rejection is on the order of 1:100. Immediately above threshold at 2.7 GeV/c, the detection efficiency for pions is approximately 50%. The EC is used both in the trigger and in offline reconstruction to select electrons, but its efficiency varies with energy. At higher energies, the EC becomes increasingly more effective at distinguishing pions from electrons, and must be relied on exclusively for confident electron identification.

The resolution of the particle mass depends on the time-of-flight measurement t, the path-length determination of the track s, and the measurement of the track momentum p. Equation 8 shows the error propagation explicitly.

$$\left(\frac{dm}{m}\right)^2 = \gamma^4 \left[\left(\frac{ds}{s}\right)^2 + \left(\frac{dt}{t}\right)^2\right] + \left(\frac{dp}{p}\right)^2 \tag{8}$$

The reconstructed mass/Z of positive particles produced from a carbon target is shown in Fig. 42. Clear peaks can be distinguished for pions, kaons, protons, deuterons, tritons, and ^{3}He. For typical flight paths of 5 m, at the three-sigma level one can distinguish pions from kaons up to 2.0 GeV/c, and pions from protons up to 3.5 GeV/c.

The timing information of the EC has an intrinsic resolution of about 0.5 ns.

A neutron candidate's velocity β is determined by dividing its path length (assuming it originated at the target) by its measured flight time. If β is significantly lower than unity ($\beta \leq 0.9$), the candidate is assumed to be a neutron, and its β is used to estimate its momentum. The determination of the velocity for neutrons also includes the uncertainty in the track length due to the unknown interaction vertex of the neutron in the calorimeter. The momentum resolution was determined using the reaction $\gamma d \rightarrow pn\pi^+\pi^-$ to tag the neutron and compare the measured momentum using the flight time with the missing momentum determined from the magnetic analysis of charged particles in the reaction [46].

The fractional momentum resolution is shown in Fig. 43 as a function of neutron momentum. At very low momenta the timing resolution degrades when very little energy is deposited in the calorimeter. Between 0.4 and 1 GeV/c, the neutron momentum is determined with an accuracy of about 6–8%. This procedure has also shown that when the EC time is calibrated using particles other than neutrons (e.g. pions or photons), the measured neutron momentum is biased and systematically underestimates the true value by approximately 10%.

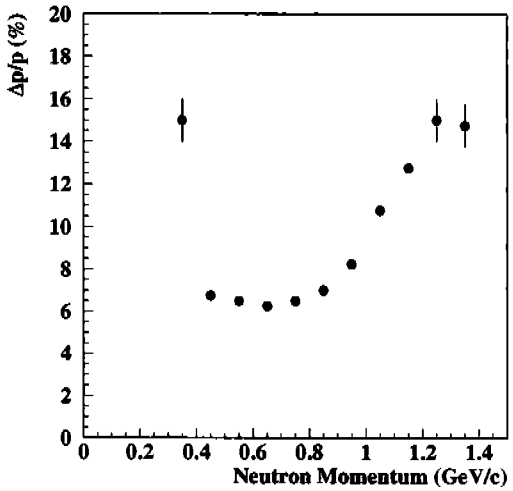

Fig. 43. Fractional momentum resolution for identified neutrons as a function of neutron momentum. The momentum is determined by measuring the flight time of neutrons from the target to the EC.

8.5 Missing Mass Resolution

Many CLAS experiments rely on the missing-mass technique to reconstruct exclusive final states. In reactions that measure all but one of the final state particles, energy and momentum conservation makes it possible to determine the mass of the missing particle. Examples for reactions where this technique

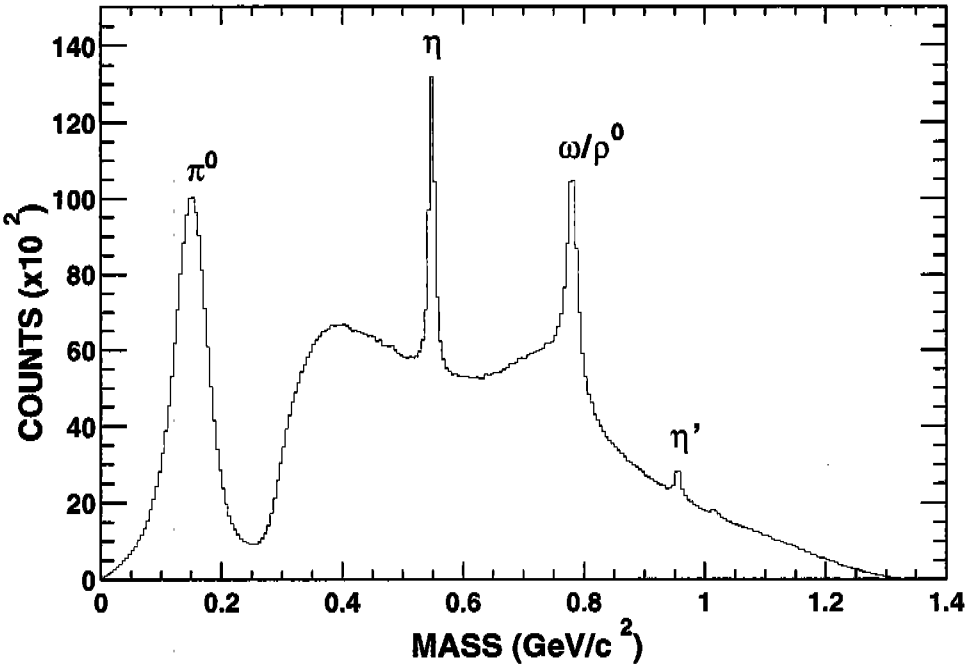

Fig. 44. Missing mass spectrum for $\gamma + p \rightarrow p + X$ showing π^0, η, and ρ/ω peaks.

is particularly useful are exclusive η and π^0 production off a proton target [47,48]. A typical example of the missing mass resolution is shown in Fig. 44, with prominent π^0, η, and ρ/ω peaks. If an electron and π^+ are detected, this method allows clean isolation of the neutron in the missing mass spectrum. This method can also be useful in the reconstruction of negative tracks with low momenta that have poor acceptance [49–51], such as in the case of K^- particles from the decay of $\phi(1020)$ mesons and excited $\Lambda(1520)$s.

Another example where the missing mass resolution can be used to isolate an exclusive final state is in the production of the Λ and Σ^0 ground state hyperons in $\gamma p \rightarrow K^+ X$ reactions. Fig. 45 shows the mass spectrum of these particles for photon energies between 1 and 2.5 GeV. Here the width of the distribution ($\sigma \approx 6$ MeV) is entirely due to the resolution of the CLAS detector.

8.6 ep Cross Section Measurement

The elastic *ep* scattering cross section was measured at a beam energy of 1.645 GeV in order to check the absolute normalization, and as a check of the detection efficiency and acceptance corrections. Cuts on the data included target vertex cuts, fiducial volume cuts, and corrections for Cerenkov counter efficiency. All detector and tracking inefficiencies were fully accounted for in the GSIM simulation that was used for the acceptance corrections. The measured

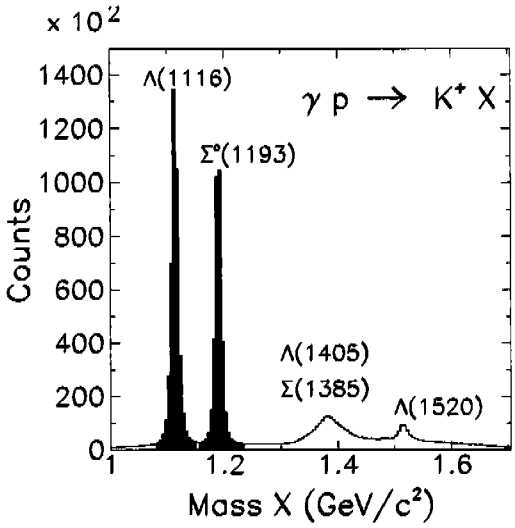

Fig. 45. Missing mass spectrum for $\gamma p \to K^+X$ showing Λ and Σ^0 peaks, as well as higher mass strange baryon resonances. The resolution in missing mass of the low-lying peaks are $\sigma_\Lambda = 6.2$ MeV and $\sigma_\Sigma = 5.8$ MeV, respectively.

cross sections are compared to established parameterizations in Fig. 46. The agreement is typically better than 3%, with occasional systematic variations as large as $\pm 5\%$.

9 Summary

The design criteria, construction details, and operational and performance characteristics of the large-acceptance CLAS magnetic spectrometer have been described. The spectrometer is used to study electron- and photon-induced reactions at the CEBAF electron accelerator. After an initial commissioning period in 1997, the spectrometer has been in routine use. All major performance goals have been met and are summarized in Table 2. The capabilities of CLAS continue to allow unprecedented exploration of the structure of mesons, nucleons, and nuclei with high luminosity and high data rates.

Acknowledgements

We would like to acknowledge the outstanding efforts of the staff of the Accelerator and the Physics Divisions at JLab that have contributed to the design, construction, installation, and operation of the CLAS detector. This work was supported in part by the Istituto Nazionale di Fisica Nucleare, the French Centre National de la Recherche Scientifique, the French Commissariat à l'Energie Atomique, the U.S. Department of Energy, the National Science Foundation,

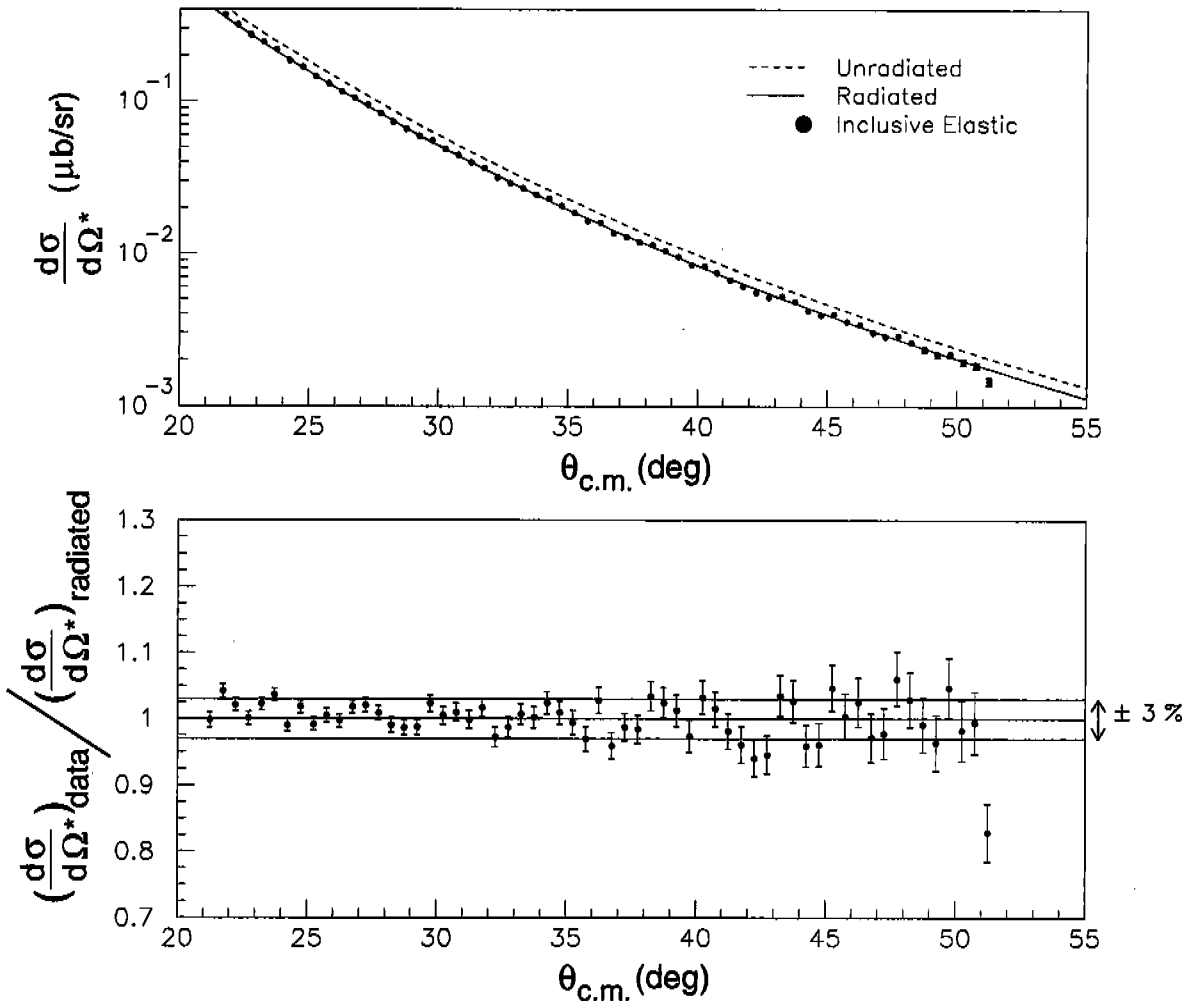

Fig. 46. Elastic cross section measurements at a beam energy of 1.645 GeV compared to the radiated (solid) and unradiated (dashed) Rosenbluth cross section using the Bosted parameterization for the form factors [52]. The experimental points are not radiatively corrected. The agreement is better than ±3%.

and the Korean Science and Engineering Foundation. The Southeastern Universities Research Association (SURA) operates the Thomas Jefferson National Accelerator Facility for the United States Department of Energy under contract DE-AC05-84ER40150.

References

[1] K. Maruyama *et al.*, Nucl. Instr. and Meth. **A376** (1996) 335.

Table 2
Summary of the CLAS detector characteristics.

Capability	Quantity	Range
Coverage	charged particle angle	$8° \leq \theta \leq 140°$
	charged particle momentum	$p \geq 0.2$ GeV/c
	photon angle (4 sectors)	$8° \leq \theta \leq 45°$
	photon angle (2 sectors)	$8° \leq \theta \leq 75°$
	photon energy	$E_\gamma \geq 0.1$ GeV
Resolution	momentum ($\theta \lesssim 30°$)	$\sigma_p/p \approx 0.5\%$
	momentum ($\theta \gtrsim 30°$)	$\sigma_p/p \approx$ (1-2)%
	polar angle	$\sigma_\theta \approx 1$ mrad
	azimuthal angle	$\sigma_\phi \approx 4$ mrad
	time (charged particles)	$\sigma_t \approx$ (100-250) ps
	photon energy	$\sigma_E/E \approx 10\%/\sqrt{E}$
Particle ID	π/K separation	$p \leq 2$ GeV/c
	π/p separation	$p \leq 3.5$ GeV/c
	π^- misidentified as e^-	$\leq 10^{-3}$
Luminosity	electron beam	$L \approx 10^{34}$ nucleon cm^{-2}s^{-1}
	photon beam	$L \approx 5 \times 10^{31}$ nucleon cm^{-2}s^{-1}
Data acquisition	event rate	4 kHz
	data rate	25 MB/s
Polarized target	magnetic field	$B_{max} = 5$ T

[2] W.J. Schwille *et al.*, Nucl. Instr. and Meth. **A344** (1994) 470.

[3] G. Audit et al., Nucl. Instr. and Meth. **A301** (1991) 473.

[4] D.G. Cassel, Proc. CEBAF Summer Workshop, Newport News, Virginia, eds: F. Gross and R. Whitney (1985) 104.

[5] K. Ackerstaff *et al.* [HERMES Collaboration], Nucl. Instr. and Meth. **A417** (1998) 230.

[6] B.D. Anderson, *et al.*, to be submitted to Nucl. Instr. and Meth. **A**.

[7] O.K. Baker, *et al.*, Nucl. Instr. and Meth. **A367** (1995) 92.

[8] M.D. Mestayer *et al.*, Nucl. Instr. and Meth. **A449** (2000) 81.

[9] D.S. Carman *et al.*, Nucl. Instr. and Meth. **A419** (1998) 315.

[10] L.M. Qin *et al.*, Nucl. Instr. and Meth. **A411** (1998) 265.

[11] G. Adams *et al.*, Nucl. Instr. and Meth. **A465**, (2001) 414.

[12] E.S. Smith *et al.*, Nucl. Instr. and Meth. **A432** (1999) 265.

[13] M. Amarian *et al.*, Nucl. Instr. and Meth. **A460** (2001) 239.

[14] M. Anghinolfi *et al.*, Nucl. Instr. and Meth. **A447**, (2000) 424.

[15] S. Taylor *et al.*, Nucl. Instr. and Meth. **A462** (2001) 484.

[16] J. O'Meara *et al.*, IEEE Trans. Magn. **MAG-25** (1989) 1902.

[17] A.J. Street *et al.*, IEEE Trans. Magn. **MAG-32** (1996) 2074.

[18] P. Rossi *et al.*, Nucl. Instr. and Meth. **A381** (1996) 32.

[19] M. Taiuti *et. al.*, Nucl. Instr. and Meth. **A357** (1995) 344.

[20] M. Ripani *et al.*, Nucl. Instr. and Meth. **A406** (1998) 403.

[21] P. Rossi *et al.*, "The photomultiplier gain monitoring system of the Large Angle Electromagnetic Calorimter for CLAS," CLAS-NOTE 2001-005, 2001.

[22] M. Taiuti *et al.*, Nucl. Instr. and Meth. **A370** (1996) 429.

[23] V. Sapunenko *et al.*, to be submitted to Nucl. Instr. and Meth. **A**.

[24] G.P. Heath, Nucl. Instr. and Meth. **A278** (1989) 431.

[25] D.C. Doughty Jr. *et al.*, IEEE Trans. Nucl. Sci. **NS-39** (1992) 241.

[26] D.C. Doughty Jr. *et al.*, IEEE Trans. Nucl. Sci. **NS-40** (1993) 680.

[27] J. Muguira, "Trigger Interactive Graphics," M.S. Thesis, Christopher Newport University, 1997.

[28] D.C. Doughty Jr. *et al.*, IEEE Trans. Nucl. Sci. **NS-41** (1994) 267.

[29] D.C. Doughty Jr. *et al.*, IEEE Trans. Nucl. Sci. **NS-43** (1996) 111.

[30] E. Jastrzembski *et al.*, Proceedings of the 11th IEEE NPSS Real Time Conference (1999) 538.

[31] CODA: CEBAF On-line Data Aquisition User's Manual, JLAB internal report, 1997.

[32] C. Cuevas *et al.*, Proceedings of the 5^{th} European Workshop on Beam Diagnostics & Instrumentation, ESRF, Grenoble, France (2001) 91.

[33] R. Nasseripour *et al.*, Bull. Am. Phys. Soc. **45**, 91 (2000); B.A. Raue, *et al.*, Bull. Am. Phys. Soc., **43** (1998) 1543.

[34] K.B. Beard *et al.*, Nucl. Instr. and Meth. **A361**, (1995) 46.

[35] J. Arrington *et al.*, Nucl. Instr. and Meth. **A311** (1992) 39.

[36] D.W. Hertzog *et al.*, Nucl.Ĩnstr.ãnd Meth. **A294**, (1990) 446.

[37] D.I. Sober *et al.*, Nucl. Instr. and Meth. **A440** (2000) 263.

[38] H. Olsen and L.C. Maximon, Phys. Rev. **114** (1959) 887.

[39] C.D. Keith *et al.*, to be submitted to Nucl. Inst. & and Meth. **A**.

[40] B. Niczyporuk, "Track Fitting in an Inhomogeneous Magnetic Field," CEBAF-PR-91-004, 1991.

[41] GEANT 3.21, CERN Program Library Long Writeup W5013.

[42] H. Egiyan, Ph.D. thesis, College of William and Mary, 2001.

[43] S.J. Taylor, "Radiative Decays of Low-Lying Excited-State Hyperons," Ph.D. Thesis, Rice University, 2000.

[44] R. DeVita, Ph.D. thesis, INFN Genova, 2001.

[45] E. Hackett and W. Brooks, "Neutron Detection in the CLAS Calorimeter: A First Measurement," CLAS-NOTE 1998-014, 1998.

[46] E. Dumonteil, G. Niculescu and I. Niculescu, "Neutron Detection Efficiency in CLAS," CLAS-NOTE 2001-006, 2001.

[47] K. Joo *et al.*, Phys. Rev. Lett. **88** (2002) 122001.

[48] R. Thompson *et al.*, Phys. Rev. Lett. **86** (2001) 1702.

[49] E. Anciant *et al.*, Phys. Rev. Lett. **85** (2000) 4682.

[50] K. Lukashin *et al.*, Phys. Rev. C **63** (2001) 065205; **64** (2001) 059901(E).

[51] S. Barrow *et al.*, Phys. Rev. C **64** (2001) 044601.

[52] P.E. Bosted, Phys. Rev. C **51** (1995) 409.